The Meteoritical Society

*Meteoritics & Planetary Science* 61, Nr 2, 241–271 (2026)
doi: 10.1111/maps.70090

# Sampling the volcanic plumes at Io: Impact speeds and shock conditions

M. J. BURCHELL [1], R. C. OGLIORE [2], and P. J. WOZNIAKIEWICZ [1]*

[1]Centre for Astrophysics and Planetary Science, School of Engineering, Mathematics and Physics, University of Kent, Canterbury, Kent, UK
[2]Department of Physics, University of Central Florida, Orlando, Florida, USA

**Correspondence**
P. J. Wozniakiewicz, Centre for Astrophysics and Planetary Science, School of Engineering, Mathematics and Physics, University of Kent, Canterbury, Kent, UK.
Email: p.j.wozniakiewicz@kent.ac.uk

*(Received 29 September 2025; revision accepted 15 December 2025)*

**Abstract**–The desire to sample material from the interior of Io, by flying through its volcanic plumes, requires consideration of the flyby speed and the types of sample collection techniques that can be utilized. Low speed collection (1–2.5 km $s^{-1}$) would require an orbit around Io itself, which is unlikely due to the accumulated radiation dose that would be experienced. Moderate collection speeds (7–9 km $s^{-1}$) are possible for flybys of Io arising from either a single passage through the Jovian system (followed by sample return) or a carefully selected orbit around Jupiter that has the main purpose of visiting Io. However, even if they include an Io close passage, most Jovian mission orbit concepts also include and even prioritize other science objectives, resulting in orbits with Io collection speeds of around 17–19 km $s^{-1}$ (or greater). Depending on the speed and collector material, the peak shock pressures during collection may thus range from 5 to hundreds of GPa for impacts on solid, nonporous media, with pressures from 0.01 to 5 GPa for impacts on low-density aerogels. These shock pressures are calculated herein for a range of Io encounter speeds and collector types, and the degree of sample capture and impact processing are estimated. While capture of material is shown to be possible at speeds up to 10 km $s^{-1}$, permitting both in situ analysis or sample return to Earth, above these speeds retention of significant amounts of unvaporized material in a collector is not viable.

## INTRODUCTION

The discovery of active volcanism on Io (Morabito et al., 1979; Smith et al., 1979) opened a new chapter in planetary geology. Tidal volcanism on Io was predicted shortly before its discovery (Peale et al., 1979), but direct observation of volcanic plumes by Voyager I provided hard evidence. Further observations were then made by subsequent space missions, such as Voyager II (e.g., McEwen & Soderblom, 1983), Galileo (e.g., see Geissler & McMillan, 2008, for a review), and New Horizons (e.g., Spencer et al., 2007). These helped build a picture of a body with hundreds of regions of active volcanism on its surface (Figure 1), which have long been taken to be the result of high-temperature silicate volcanism (e.g., McEwen et al., 1998). Recent observations from the Juno spacecraft report 343 hot spots on the surface of Io (Davies et al., 2024), and the latest Juno findings suggest these are fed from local magma sources and not an internal, shallow, global lava ocean (Park et al., 2025). A detailed review of the structure and composition of Io can be found in Lopes et al. (2023).

Taken together, this suggests a long history of continuous volcanic activity on Io, with 3% of the surface covered with recent or currently active volcanoes (Davies et al., 2024), many of which produce plumes up to 500 km high (see Davies & Vorburger, 2022, or de Pater et al., 2023, for a recent review). It thus becomes tempting for future space missions to plan deliberate flights through the plumes to sample the gas, dust and plasma contents.

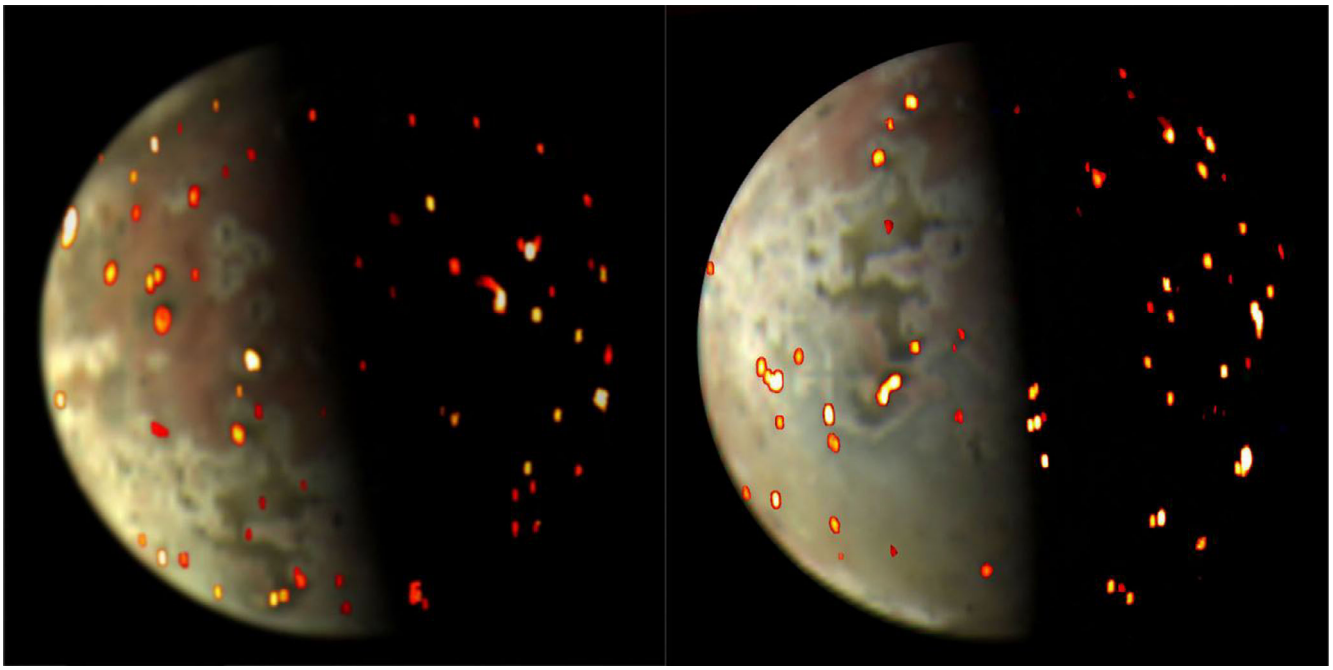

FIGURE 1. Io in optical and infrared with overlaid hotspots as imaged by the NASA Juno mission's JIRAM (Jovian Infrared Auroral Mapper) instrument. Image credit: NASA/JPL-Caltech/SwRI/ASI/INAF/JIRAM, image source: NASA photo gallery image PIA25888. (Color figure can be viewed at wileyonlinelibrary.com)

However, the plumes have, to an extent, already been sampled. In 2001, during an encounter with Io, the Galileo spacecraft accidentally flew through an unexpected volcanic plume (Thor), detecting clusters of what were identified as $SO_2$ ions (Frank & Paterson, 2002). Furthermore, submicron dust coming from Jupiter was measured in interplanetary space by the Ulysses spacecraft (Grün et al., 1993), and data from the Galileo spacecraft identified this as coming from Io's volcanic plumes (Graps et al., 2000). Analysis of impact mass spectra of small particles in the Jovian dust streams (obtained by the Cassini spacecraft during its flyby of Jupiter in 2000) also indicated a composition compatible with an Io origin (Postberg et al., 2006). But these measurements only indicate the possibilities that would arise with a dedicated sampling mission. It is therefore no surprise that mission proposals for Io are regularly made which envisage close engagements with the volcanic plumes.

The volcanic plumes at Io are often characterized by type. Here, the focus is on the tall, dust and gas rich plumes, observation of which were the first indication of active volcanism on Io (Morabito et al., 1979). Early on, an attempt was made to split these plumes into two groups, with names based on the archetypal example of each, Prometheus and Pele (McEwen & Soderblom, 1983). Prometheus-type plumes (the most common) are some 100 km tall and are dust rich with eruption speeds of approximately 0.5 km $s^{-1}$, whereas Pele plumes reach 300+ km heights and have a more gas rich composition with 1+ km $s^{-1}$ eruption speeds (Davies, 2007; Geissler & McMillan, 2008). Prometheus-type plumes are often long lived (multiple years, with the archetypal Prometheus plume itself observed in every set of relevant spacecraft observations to date—a period spanning over 45 years), with Pele-type typically being of shorter duration (although the archetypal Pele plume itself has been observed since the Voyager era). However, it should be noted that there are a range of plumes of each type (and indeed not all active volcanic sites are associated with plumes), and it is possible that what appear to be separate classes may be subsamples of a continuum.

While longevity and height are essential plume properties required for mission planning, another key property is the dust content (to permit an estimate of the amount of material to be collected per plume passage). Optical observations of plumes are of some use, but their interpretation often relies on application of Mie scattering techniques, which are not sensitive to the presence of larger grains. Models based on the plume eruption mechanism are therefore also used to give the maximum particle size at different altitudes (i.e., flyby encounter distances). If one considers launch of particles from a volcanic vent at the surface, Lorenz (2015) calculates a maximum particle diameter at 100 km altitude of approximately 70 μm in Io's Pele plume. It should be noted that there is an error in Lorenz (2015)

concerning the relevant calculation of the total column density of 70 μm particles: instead of a column density of the reported $5 \times 10^3$ 70 μm pyroclasts per $m^{-2}$ for the Pele plume, the model described in Lorenz (2015) (equation 3) actually predicts $2.5 \times 10^6$ pyroclasts per $m^2$ (assuming a plume dust/gas ratio of 0.1). For 70 μm porous silicate particles of density 1.8 g $cm^3$, this corresponds to a collected mass of 80 mg in a Stardust-sized collector of area 0.1 $m^2$ (Tsou et al., 2003) flown through the Pele plume at an altitude of 100 km. One can also consider the size distribution of pyroclasts injected into the plume, where, for example, Ogliore and Wilson (2025) estimate that the pyroclasts in the Prometheus plume have a normal size distribution with a peak at 25–30 μm diameter, and a tail which extends slightly beyond 100 μm. Either way, the estimated size distribution for these particles indicates that the plumes will contain a significant number of particles greater than a micron in size (as well as the submicron scale material sampled in impact ionization), and which, depending on the density at a given altitude, will be available for collection.

Of crucial importance to any Io plume sampling mission are key encounter parameters, such as the sampling altitude (which determines the size distribution) and the impact speed (which will influence any alteration of the sample during capture). In this paper, we thus consider the relevant Io plume-spacecraft impact speeds and altitudes, and what these imply for the necessary sampling techniques.

## TYPES OF ORBIT

There are several types of spacecraft trajectories that could provide access to the plumes at Io (see Figure 2). Spacecraft on heliocentric bound orbits, or on interstellar unbound trajectories intending to leave the Solar System, can be targeted to pass close by Io. While there are currently no cases of a Jovian space mission with the former trajectory, in the latter case, the Pioneer 10 and 11, Voyager I and II, and New Horizons spacecraft have all been able to report data on Io, see Table 1, with initially radio occultation data from Pioneer 10 and the first visual image from Pioneer 11.

Spacecraft have also entered orbit around Jupiter, that is, in a Jovian-bound orbit, permitting either distant observations of Io from elsewhere in the Jovian system, or close fly-bys of Io. Missions on Jovian Bound Orbits that have included close encounters with Io and yielded Io data are Galileo and Juno, with Europa Clipper and JUICE enroute (and which will provide distant Jovian Bound Orbit encounter data for Io).

A fourth orbit type is also possible, that is, an Io Bound Orbit (either elliptical or circular). However, while tempting for reasons of sustained closeness to the target body, in the case of Io this is made problematic not just by orbital perturbations due to Jupiter but also by exposure to the harsh local radiation environment. The expected radiation dose is so severe that it will likely damage flight electronics, rendering such a mission difficult to envisage. Detailed dose calculations for different types of orbits are given, for example, in Adams et al. (2012), with a fuller discussion of the radiation environment at Io given in Bagenal and Dols (2020). A spacecraft on a Jovian Bound Orbit which passes close to Io still experiences this radiation environment, but only during the short period of close encounter, reducing the accumulated dose to a more practical level which can be allowed for with appropriate spacecraft design engineering (e.g., including a radiation vault, as used by Juno).

Only two of these orbit types (Interstellar Unbound Trajectories and Jovian Bound Orbits) have so far been utilized (with key parameters given in Table 1) but all four orbit types are considered herein for completeness. In the following sections, more details of the typical orbits and resultant Io plume encounter speeds are given.

## ENCOUNTER SPEEDS

The encounter speed at Io is vital when considering the outcome of the encounter with a plume particle, yet it is often not stated in published work. The situation is more complicated for sample capture, as different sample capture techniques (see later discussion) perform better at different encounter speeds, for example, intact capture which occurs at intermediate speeds (few km $s^{-1}$) versus impact ionization which is better at high speed (>5 or 10 km $s^{-1}$). The encounter speeds are thus considered here by orbit type, with results indicating a wide range of values that are possible, even for a single type of orbit (see Table 2 for a summary).

### Interstellar Unbound Trajectories

Starting with Interstellar Unbound Trajectories, the spacecraft on such orbits can be passing through the Jovian system, deliberately using the Jovian encounter to adjust their speed and trajectory. Therefore, the speed relative to Io should be considered as variable, dependent on what stage of the passage near Jupiter the observations are made at. The result is that Io encounter speeds of up to some 30 km $s^{-1}$ are feasible.

### Heliocentric Bound Orbits

For Heliocentric Bond Orbits (i.e., without Jupiter capture), the Io encounter speed as estimated by Davis et al. (2024) for the proposed Prometheus D mission is

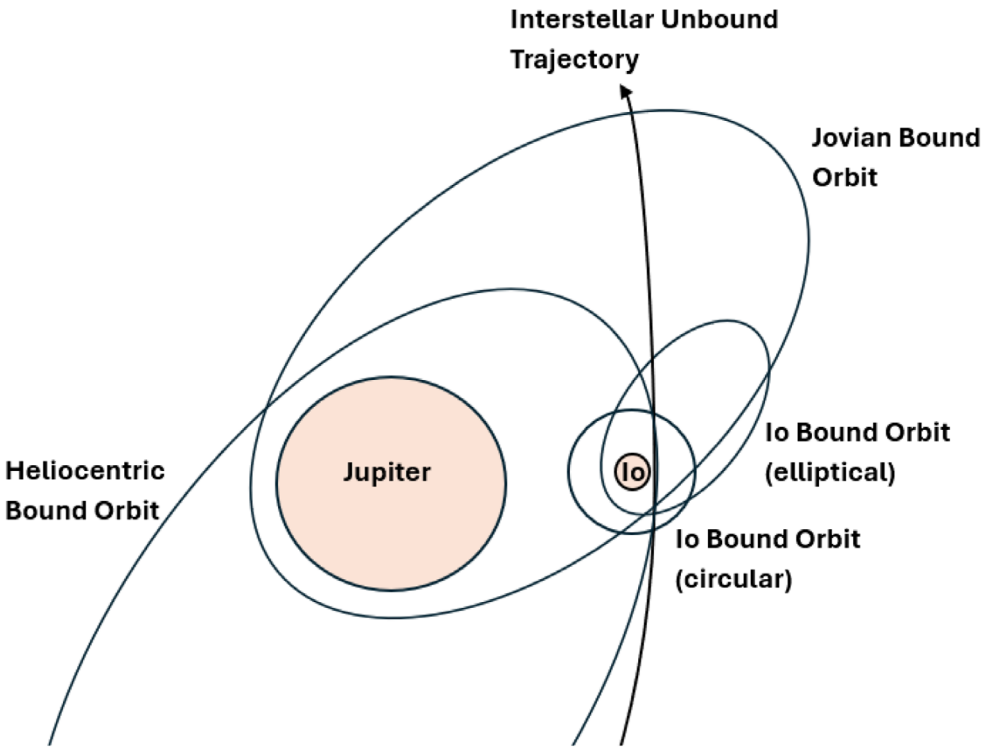


FIGURE 2. Types of orbit (not to scale) for exploring Io: Heliocentric bound orbits, interstellar unbound trajectories, Jovian bound orbits, and Io bound orbits (where both the circular and elliptical cases are shown). (Color figure can be viewed at wileyonlinelibrary.com)

TABLE 1. Space missions observing Io (past, present and currently enroute).

| Type of orbit | Space mission | Encounter date(s) | Encounter altitude (km) | References |
|---|---|---|---|---|
| Interstellar Unbound Trajectory | Pioneer 10 | 1973 | 357,000 | Anderson et al. (1974), Kliore et al. (1975) |
| | Pioneer 11 | 1974 | 314,000 | https://www.nasa.gov/history/45-years-ago-pioneer-11-explores-jupiter/ |
| | Voyager 1 | 1979 | 20,600 | Morabito et al. (1979), Stone and Lane (1979) |
| | Voyager 2 | 1979 | 1,130,000 | Stone and Lane (1979), McEwen and Soderblom (1983) |
| | New Horizons | 2007 | 2,239,000 | Spencer et al. (2007) |
| Jovian Bound Orbits | Galileo | 1995–2003 | 102 to >300,000 | Geissler and McMillan (2008) |
| | Juno | 2017–2025 | 1500 to >100,000 | Davies et al. (2024) |
| | Europa Clipper | Launched 2024 | Arrive at Jupiter 2030 | Pappalardo et al. (2024) |
| | JUICE | Launched 2022 | Arrive at Jupiter 2031 | Grasset et al. (2013) |

*Note*: Spacecraft trajectories are defined as: interstellar unbound trajectory or Jovian bound orbit (see Figure 2).

9 km $s^{-1}$ (at an altitude of 10 km), for a feasible mission profile with minimal requirements on $\Delta v$, launch mass, etc. Such a mission would reduce the radiation dose on the spacecraft, but would involve a single transit of a plume at Io, hence the need for as low an altitude as possible to accumulate as much material as it can in one go.

## Jovian Bound Orbits

If Jupiter capture occurs, then a range of Jovian Bound Orbit type orbits are possible which either bring a spacecraft close to Io, or which permit observations from a distance. To date, Jovian missions typically favor a wide range of science objectives (and not just Io observations)

TABLE 2. Summary of estimated dust capture speeds in encounters at Io.

| Orbit type | Speed (km $s^{-1}$) |
|---|---|
| Interstellar Unbound Trajectory | Up to 30 |
| Heliocentric Bound Orbits | 9 |
| Jovian Bound Orbits | 7–30, with 17–19 typical |
| Io Bound Orbits | 1.5–1.8 (circular)<br>1.45–2.4 (elliptical) |

and leave the close approaches at Io to the end of the mission, thus minimizing the radiation dose which may compromise the mission until near the mission end.

A range of Jovian Bound Orbits which involve Io observations are thus achieved, even inside a single mission. For example, Galileo had seven close encounters with Io (altitudes less than 1000 km), four near-distant sets of observations (altitudes 45,800–252,000 km) and several more distant passes—for a full list of all Galileo encounters with Io, see table 3.2 in Perry et al. (2007).

More recently, Juno has also had various encounters with Io, again leaving the close ones to the later mission phases to reduce the hazard to the spacecraft from the accumulated radiation dose. Juno achieved this by varying its orbit during its mission. During its main mission at Jupiter (2015–2021), Juno had a nominal 53-day orbit, with perijove at 4163 km and apojove at 8.03 million km. The apojove of Juno's orbit was then systematically reduced to 5.93 million km by repeated close encounters (and hence near observations) with the Galilean satellites Ganymede, Europa, and Io, reducing the Jovian orbital period to some 33 days. This then permitted several close encounters with Io in late 2023 and 2024, with a closest approach of less than 1500 km. Juno now (2025) focuses on Jovian observations, aided by movement of the perijove position relative to Jupiter to provide different views of the planet.

The actual Io encounter speed of a spacecraft (in an Io-centric frame) on a Jovian Bound Orbit is a combination of the spacecraft's speed in its Jovian orbit and Io's orbital speed (in a way dependent on the relative angle at encounter) with a further contribution from Io's gravitational attraction on the spacecraft and is thus specific to a particular encounter. For example, Galileo's encounter speed at Io during its I31, 2001, passage over the Io north pole (with a minimum altitude of 194 km) was 7 km $s^{-1}$ (Frank & Paterson, 2002). Higher speeds are also possible, especially given Io's mean Jovian orbital speed of 17.3 km $s^{-1}$ and the need for elliptical Jovian orbits to reduce radiation flux experienced by the spacecraft. Thus, Juno's closest passages to Io (1500 km altitude) in 2023 and 2024 had a relative encounter speed of approximately 30 km $s^{-1}$ (Park et al., 2025). Predictions of encounter speeds for future close observation or sampling missions on a Jovian Bound Orbit mission profile range from 7 km $s^{-1}$ for Prometheus-NF (at altitudes of 10–50 km, Davis et al., 2024) to 17–19 km $s^{-1}$ for Io Volcano Observer (IVO) (with a lowest Io altitude some 50–200 km depending on mission profile, McEwen et al., 2021). Note that the Prometheus-NF proposal is in effect a hybrid mission, with capture into Jovian orbit for a 3.3-year mission, followed by an escape maneuver to launch the spacecraft on an Earth-crossing heliocentric orbit for a sample return to Earth.

Other estimates also exist for the Io encounter speed in a Jovian Bound Orbit. For example, Lorenz (2015), who considered the hazard to a spacecraft from flying through a plume at Io, used an assumed typical encounter speed of 18 km $s^{-1}$.

## Io Bound Orbits

The final type of orbit is the Io Bound Orbit, either circular or elliptical. Although, as already noted, it is not likely to be of practical use due to the radiation dose that would be accumulated, these are included here for completeness. Other problems with Io bound orbits include the necessary $\Delta v$ to achieve the orbit (which requires a large mass of propellant) and the perturbing influence of Jupiter on the orbit, which would likely be stable for only up to 7–21 days unless the spacecraft repeatedly corrected for this (e.g., McEwen et al., 2023).

Taking the case of a circular orbit first, the orbital speed versus altitude is shown in Figure 3, and for Io is in the range of 1.5–1.8 km $s^{-1}$ for altitudes below 1000 km which are suitable for sampling plumes. Speeds at similar altitudes for the other Galilean satellites are also shown for comparison. The variation between satellites in the speeds at a given altitude reflects the different sizes, masses, and densities of the various bodies (see Figure 4). Although Io is the second smallest, it has the highest density, being rocky with a metal core. Europa also has a mostly rocky and metal-rich core and hence high density, despite having an icy surface. By contrast, although Ganymede and Callisto are similar in many ways, the former is both larger and denser than the latter, resulting in an almost 40% greater mass. It is these differences in basic properties that explain the variation in orbital speed with altitude between the Galilean satellites.

In an elliptical orbit, speeds at a given altitude depend on both the altitude and the apogee of the orbit. Here, we assume the perigee (i.e., lowest point in the orbit) is the altitude at which sampling will occur, and give the speed at perigee for a range of apogee values at Io in Figure 5a. Again, similar values for the other Galilean satellites are shown in Figure 5b–d for comparison. At Io, for plausible sampling altitudes, it can be seen that the apogee dependent perigee speeds range from some 1.45–2.4 km

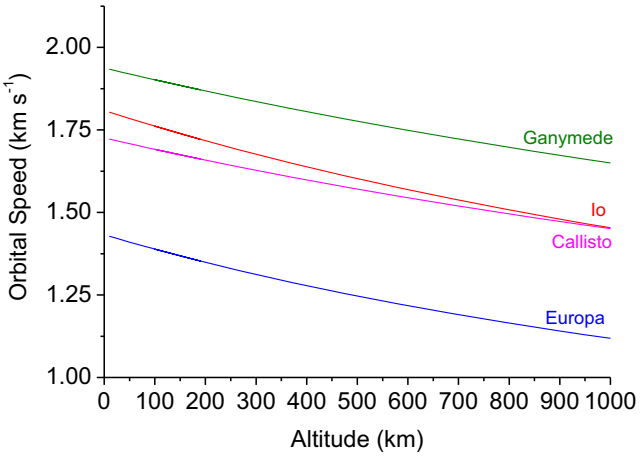


FIGURE 3. Spacecraft orbital speed at Io in a circular Io Bound Orbit, as a function of altitude. Similar orbital speeds at Europa, Ganymede, and Callisto are shown for comparison. (Color figure can be viewed at wileyonlinelibrary.com)

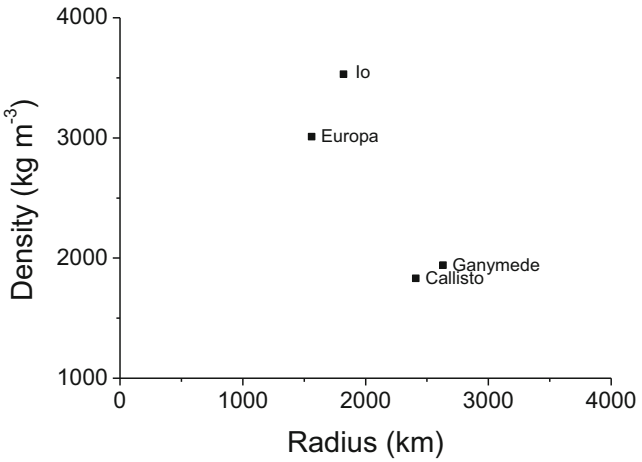


FIGURE 4. Mean radius versus density of Io, Europa, Ganymede, and Callisto.

$s^{-1}$. Similar speed ranges are seen at the other Galilean satellites, with slightly lower absolute values at Europa and greater values at Ganymede.

## COLLECTOR TECHNOLOGIES

There are several ways to measure dust in space. One approach is to measure flux versus size and speed. A simple such measurement method, for example, is a metal plate equipped with piezo-electric acoustic sensors, which respond to high-speed impact. If charge sensing grids are arranged above such a plate, the impact speed and location can be found, and combined with the piezo-electric sensor signals to obtain a measure of impact mass. Such detectors have a long heritage in space, and a current example is DISC on the Comet Interceptor mission (Della-Corte et al., 2023). If the impact speed is determined by the spacecraft encounter speed, and there are sufficient piezo-electric sensors to triangulate impact locations, it could be argued that the charge sensing grids are unnecessary. But measuring particle charge itself would still be of interest, so charge sensors should be retained.

However, as well as measuring the flux, a key goal for a more detailed study is the composition, determined either in situ or via collecting samples for return to Earth.

There are various types of instruments that can be used to collect or sample small particles in space for compositional analysis (e.g., see Wozniakiewicz et al., 2021, or Burchell & Wozniakiewicz, 2024), and these are summarized in Table 3. Several basic divisions can be made. The first crucial one is whether in situ or postflight analysis is planned. In the former case the collected material has to be processable/analyzable on-board, which limits the applicable analysis techniques. Probably the best known type of the former is the impact ionization time-of-flight (TOF) mass spectrometer, for example, the Cosmic Dust Analyzer (CDA) on the successful Cassini mission to Saturn (Srama et al., 2004), or the Surface Dust Analyzer (SUDA) on the Europa Clipper mission launched in 2024 (Kempf et al., 2025). In such an instrument, the impact of a small (typically submicron) dust particle at high speed (above a few km $s^{-1}$) produces a plasma, whose ion content is accelerated rapidly in a strong electric field and which then drifts to a charge detector. This produces a TOF mass spectrum. By contrast, passive types of collector rely on capturing the impactor or its residue (using, e.g., aerogels, capture cells, metal foams, and thin foils or thick metal targets), and then returning the samples to Earth for detailed analysis postflight. This permits a much wider range of sample analyses. Examples of various passive capture media are shown in Figure 6.

It should be noted, however, that the various passive collection options can serve both in situ and postflight analysis needs if chosen appropriately. For example, the proposed sample collection missions at Enceladus rely on in situ analysis even for the passive collectors (e.g., see Burchell & Wozniakiewicz, 2024). However, as stated, the sample-return approach permits a wider range of analysis techniques to be employed, many of which cannot be deployed on spacecraft due to size, mass and/or volume constraints, or which can only operate with reduced sensitivity. Key characteristics of the various sampling techniques in Table 3 are summarized below, with an emphasis on the degree of sample alteration during capture, since this has important implications for any subsequent analysis.

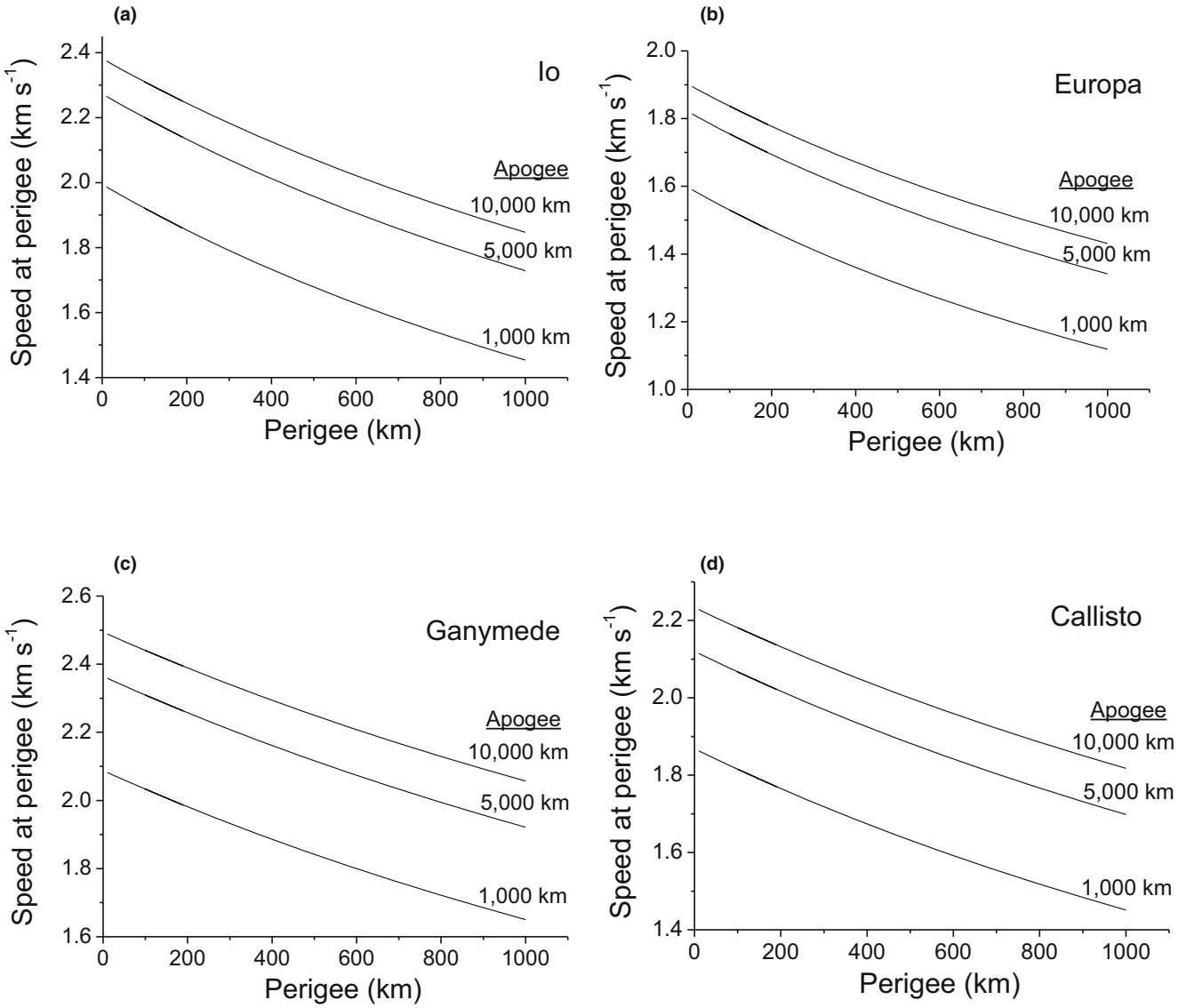


FIGURE 5. Speed at perigee for a range of apogee altitudes for the Galilean satellites: (a) Io, (b) Europa, (c) Ganymede, and (d) Callisto.

**Impact Ionization**

In impact ionization TOF mass spectrometers, the sample is not collected for future analysis. Instead, the collection method vaporizes the sample (via impact on a metal surface) and the built-in electric accelerating and focusing fields provide a TOF spectrum where, assuming singly charged ions, the time of flight is directly related to ion species mass. The resulting mass spectrum is, however, highly sensitive to the impact speed. The observed ion yield may also have a weaker dependence on other parameters, such as particle surface roughness, detector noise levels, and detector sensitivity.

There have long been reports from laboratory experiments that impacts can produce ionization signals at low speed (e.g., Bedford, 1971), but it is thought this is a surface charge effect where the impactor is a charged particle that was accelerated in an electrostatic accelerator. For example, if the charge on the projectile is removed after acceleration, the degree of observed ionization significantly decreases (Burchell, Cole & McDonnell, 1998). Here, however, it is the impact plasma produced from the bulk impactor that is of interest, and there is a lower impact speed threshold to observe such spectra. Below typically about 2 km $s^{-1}$, no significant volume of charged ions is produced from the impactor in the impact, so there are no relevant mass spectra to observe.

As impact speed increases, both easily ionized metals (such as K and Na, often present in experiments as surface contaminants) and large molecular fragments are first

TABLE 3. Typical dust sampling or collector technologies.

| Type | Characteristics | Particle size and speed range | Example references |
|---|---|---|---|
| Aerogel | Porous media into which particles tunnel and are collected semi-intact | >0.2-μm size<br>Up to ~10 km $s^{-1}$ for semi-intact capture, with increasing damage up to 15 km $s^{-1}$ | Burchell, Thomson, and Yano (1998); Burchell, Graham, and Kearsley (2006); Burchell, Fairey, et al. (2008); Hörz et al. (2006); Postberg et al. (2014); Yamagishi et al. (2021) |
| Capture cell | Thin layer (to disrupt impactor) in front of solid substrate to capture residue | >Micron size<br>Up to ~10 km $s^{-1}$ | McDonnell et al. (1984); Yano et al. (1997); Kearsley, Graham, et al. (2005); Dignam et al. (2022); Wozniakiewicz et al. (2019) |
| Metals | Either thin foils or thick, effectively semi-infinite, targets, where impacts result in holes or craters, possibly lined with residue | 10s of nm to mm size<br>Speeds up to 8 or 10 km $s^{-1}$ before all residue is lost (vaporized) | Laurance and Brownlee (1986); Love and Brownlee (1993); McDonnell et al. (1995); Yano et al. (1997); Burchell, Foster, et al. (2008); Kearsley et al. (2008); Price et al. (2010); Kearsley et al. (2024) |
| Metal foams | Open pore foamed metals into which particles tunnel on impact with a high degree of disruption but where the fragments are contained in the target | Up to few mm size<br>Up to 10 km $s^{-1}$ | Ryan and Christiansen (2015); Cherniaev (2021) |
| Silicon and germanium wafers | Ultrapure targets, ideal for small impactors | Submicron to few 10s of microns size.<br>High speed | Simon et al. (1991); Graham, Kearsley, et al. (2001); Graham et al. (2004); Taylor et al. (2001); Price et al. (2014) |
| Solar cells | Large area targets retrieved from Earth Orbit, but with complicated structure making composition analysis hard | Micron and above.<br>Speeds up to 8 or 10 km $s^{-1}$ before all residue is lost (vaporized) | McDonnell et al. (1995); Paul et al. (1997); Graham et al. (1999); Kearsley, Drolshagen, et al. (2005); Olivieri Lorenzo et al. (2024) |
| Impact ionization mass spectrometers | The impact on an ultrapure metal target produces an ionized plasma, which is then accelerated by a large electric field to produce a time of flight mass spectrum | 10 nm to few microns size.<br>>2 km $s^{-1}$, but response is highly impact speed dependent | Kissel et al. (1986); Kissel and Krueger (1987); Goldsworthy et al. (2003); Kissel et al. (2003); Srama et al. (2004); Hillier et al. (2012); Pappalardo et al. (2024) |

*Note*: Example references are given, but there are many more in the literature.

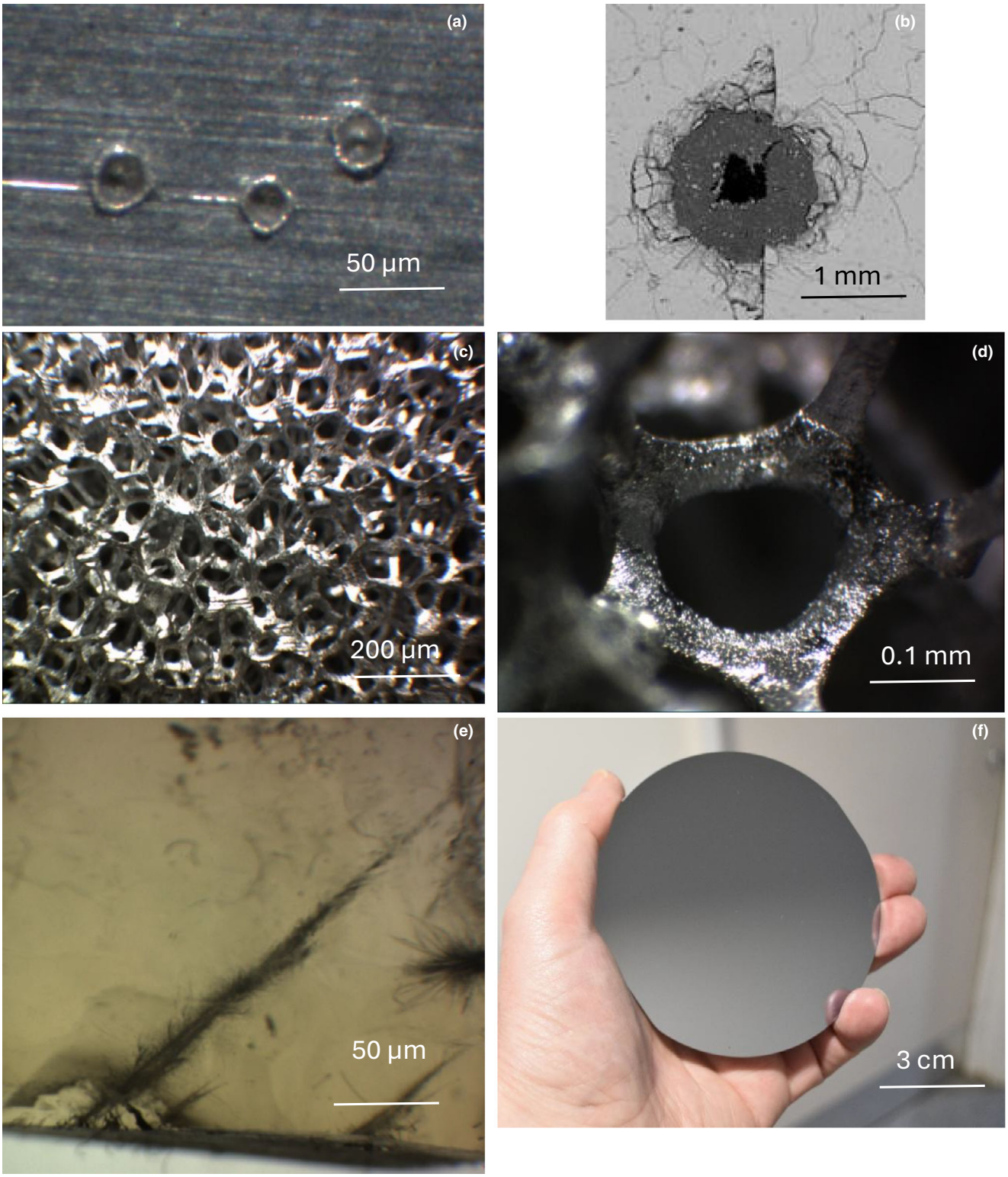


FIGURE 6. Examples of various sample collector materials. (a) Craters on an aluminum foil from impacts by soda-lime glass beads (22.8 μm diameter) at 7.65 km $s^{-1}$. (b) Crater from impact of a kamacite particle (125–250 μm diameter) on a solar cell at 5.35 km $s^{-1}$ (Burchell et al., 2012). (c) Metal (aluminum) foam showing overall structure of pores and ligaments. (d) Metal (aluminum) foam showing close up of one pore and surrounding ligaments. (e) Track in aerogel (96 kg $m^{-3}$) after an inclined impact (from bottom left) of an enstatite grain 125–150 μm in diameter. (f) A 10-cm diameter silicon wafer. (Image sources: Unless otherwise specified were Univ. of Kent). (Color figure can be viewed at wileyonlinelibrary.com)

TABLE 4. Thresholds for producing ions in impact ionization measurements of Fe, Al, and C projectiles impacting various targets (Ratcliff, Reber, et al., 1997).

| Projectile material | Target material | Threshold speed (km $s^{-1}$) |
|---|---|---|
| Fe | Rh | Fe: 15–16; Rh:15–16 |
| Fe | Al | Fe: 8 ± 3; Al: 8 ± 3 |
| Fe | Mo | Fe: 8 ± 3; Mo: 8 ± 3 |
| Fe | Au | Fe: 15 ± 2; Au: n.o. |
| Fe | Ag | Fe: 10 ± 5; Ag: 10 ± 5 |
| Fe | Cu | Fe: 7.7–8.4; Cu: 8.4–8.7 |
| Al | Co | Al: 21 ± 5; Co: 21 ± 5 |
| Al | C | Al: 20 ± 5; C: 19 ± 2 |
| Al | Fe | Al: 18 ± 5; Fe: 22 ± 5 |
| C | Fe | C: 16 ± 2; Fe: 15 ± 4 |

Abbreviation: n.o., not observed in the data set.

produced. The typical ion mass then gets smaller as the impact speed increases until purely atomic species are formed (e.g., Dalmann et al., 1977; Fiege et al., 2014; Goldsworthy et al., 2003; Hillier et al., 2012, 2018). This process is material dependent and requires laboratory calibration. For example, Dalmann et al. (1977), reported from laboratory experiments that the relative intensity of various ion species in impacts of Fe on Au changed strongly as impact speed increased from 2 to 10 km $s^{-1}$. They found that at low speed the mass spectra were dominated by the low ionization potential metals Na and K. The relative intensities then changed with increasing speed, with the Na and K relative content falling and the Fe content increasing. Later, Ratcliff, Burchell, et al. (1997) showed that in such impacts the absolute (and not just the relative) yield of Fe increased significantly with increasing impact speed.

The associated threshold impact speed for ionization also depends on the projectile:target combination (e.g., see Table 4 here and Ratcliff, Burchell, et al. 1997; Ratcliff, Reber, et al. 1997 for a discussion). For example, in Table 4 it can be seen that the impact speed to produce an observable Fe signal from impact by an Fe projectile can vary by as much as a factor of two depending on the composition of the target. Furthermore, from Table 4 it can also be seen that the impact speed thresholds for the materials involved depend on which is the target and which the projectile, that is, Al impacting Fe is not the same as Fe impacting Al.

The sensitivity of the detectors used in such measurements has to be allowed for, however, and the apparent threshold may actually be indicative of a jump from a very small signal to a larger one, rather than an absolute absence below the thresholds given in Table 4. This is illustrated by Fiege et al. (2014) who reported on impacts of orthopyroxene on a Rh target. They observed that, in relative units, a signal for Rh was barely observable (<<1 unit of intensity) for impact speeds <4.9 km $s^{-1}$, had reached an intensity of 2 at 5–10 km $s^{-1}$, an intensity of 30 at 10–15 km $s^{-1}$, 100 at 15–20 km $s^{-1}$, 200 at 20–25 km $s^{-1}$, 400 at 25–30 km $s^{-1}$, and reached 700 at 30–35 km $s^{-1}$. By contrast, Ratcliff, Reber, et al. (1997) reported a threshold for Rh in impacts by Fe at 15–16 km $s^{-1}$. This corresponds to a speed regime in Fiege et al.'s results where a large increase was observed in the Rh signal. Since there is Fe in pyroxene, the presence of Fe in the resulting impact mass spectra can also be observed in the results of Fiege et al. (2014). They reported that Fe was not observable below 4.9 km $s^{-1}$, had a small intensity (2 unit) signal from 5 to 10 km $s^{-1}$, and had an intensity of 10 for speeds above 10 km $s^{-1}$. When compared to the results of Ratcliff, Reber, et al. (1997), reported above which found a threshold for Fe of 15–16 km $s^{-1}$, this suggests that where the element is present (target/projectile) may be influencing the results. Indeed, it has been observed that when olivine and magnesite were used in a single experimental set-up, the impact speed threshold for observing Fe in 50% of spectra was 5 and 10 km $s^{-1}$, respectively (Hillier et al., 2018). This suggests that the way an element is bonded in a mineral influences its presence in an impact TOF mass spectra. Careful calibration of such instruments is thus required using a range of minerals and, where appropriate, organic impactors. Key to this type of work are laboratory experiments which use projectiles of representative composition (and not just simple metals which are easily charged). This can be achieved for a wide range of materials by coating them with conducting layers, either polymers (e.g., Goldsworthy et al., 2003; Burchell & Armes, 2011; Chan et al., 2021, 2023; Mikula et al., 2024; see Fielding et al., 2015, for a review) or metals (e.g., Fiege et al., 2014; Hillier et al., 2012, 2018).

Of particular relevance to Io, is detection of sulfur in impact ionization TOF mass spectrometry. Observation of atomic sulfur lines have been reported by CDA analyzing the Jovian dust streams, and indeed this was used to identify the grains coming from Io (Postberg et al., 2006). However, no systematic laboratory study appears to have been undertaken, although model microparticles containing sulfur have been developed and accelerated to hypervelocities (Fujii et al., 2006).

Although not expected to dominate at Io, ice may be present as condensates in the Io plumes, and is also relevant to passage near other Jovian satellites. Ice has been studied in impact ionization experiments. Ice particles can be produced by electrospray production of charged ice grains which permits their acceleration in electrostatic accelerators (e.g., see Burke & Continetti, 2024, for a review). Using such ice grains doped with

amino acids, it has been reported that the presence of characteristic amino acid related peaks can be observed in TOF mass spectra for impacts at 3–4 km $s^{-1}$, but that the yields are influenced by salt concentrations in the ice grains (Burke et al., 2023). Higher speed impact studies with ice await use of greater accelerating voltages.

Impact induced ionization has been reported for the inverse process of metal (Fe projectiles) impacting ice targets at up to 60 km $s^{-1}$ (Burchell et al., 1996; Timmermann & Grün, 1991), but a detailed analysis of the associated mass spectra of doped ice targets is lacking. An alternative approach has been to use laser irradiance of doped ice targets to simulate impacts and to observe the mass spectra produced (e.g., Postberg et al., 2018). This latter method allows study of the way molecular fragments form when the parent molecules break apart.

Nevertheless, despite the issues described above, several crude schemes exist to try to characterize the degree of molecular fragmentation versus impact speed. Based on experiments, a simple scheme has been proposed by many, including Collette et al. (2014) and Hillier et al. (2018). At low speeds (5–10 km $s^{-1}$), the impact plasma is dominated by neutral species and easily ionized atoms and molecules (with large molecular fragments). Then, at 10–20 km $s^{-1}$ more elements and fewer large molecular fragments are present. Finally, above 20 km $s^{-1}$ the plasma is dominated by neutrals and ionized atoms (e.g., Collette et al., 2014 report complete vaporization above 20 km $s^{-1}$). This, however, hides a great deal of detail reported in the wider literature, and a flavor of this greater detail is summarized in Table 5. In general, the mass spectra from a single impactor (mineral or organic dominated) depend both greatly upon impact speed and the precise nature of the impactor. These differences are not just between the general classes of mineral versus organic, but also inside each class, for example, between aromatic and aliphatic organics depending on thermal fragility etc. Clearly, the mass spectra are strongly dependent on impact speed, and the various speed regimes cover the range expected for different types of Io encounters.

It should also be noted that impact ionization can produce both cations and anions, at different ratios that are species dependent. For example, Dalmann et al. (1977) observed with iron projectiles that anions were produced at a rate of only 3%–6% of that of cations. However, as often reported, for example, Hillier et al. (2018), this is strongly dependent on the material being studied, and for example, organics often prefer anion formation. Therefore, the science goal and the materials it is planned to collect (metals and minerals versus organics) should determine the mode of operation of an impact ionization detector (cation versus anion detection).

The active area of a TOF impact mass spectrometer has traditionally been small. For example, CIDA (Kissel et al., 2003) deployed on the NASA Stardust mission to comet Wild-2 (launched 1999) had a usable area of some 8 $cm^2$ (when allowance is made of the inclination of the target to the incoming particle direction), and CDA (launched 1997) had an active TOF mass spectrometer surface area of some 160 $cm^2$ (see Grün et al., 2000, for a discussion). A more recent example of such an instrument is SUDA on the Europa Clipper mission (launched 2024), which has an active surface area of 220 $cm^2$ (Kempf et al., 2025). The particle size these instruments are sensitive to is limited to small grains of dust. SUDA, for example, was calibrated for impacts by particles in the size range 22 nm to 2.7 μm (Kempf et al., 2025). They are well suited to either high flux environments or extended continual sampling of low flux sources, and in both cases fine particulates are required.

## Passive Dust Collectors

There is a wide range of materials that can be used for this purpose. The main ones are briefly described below.

### *Metals*

The simplest dust collector is a metal plate, typically of thickness at least 10x the maximum expected impactor diameter. A sequence of impact outcomes can be constructed versus impact speed. For example, in ductile target materials, rebound occurs at low speed (typically less than 500 m $s^{-1}$ or so, but can still occur at 1 km $s^{-1}$ depending on the projectile materials involved). This is followed by sticking (few 100 m $s^{-1}$ to 1 km $s^{-1}$) and then cratering (>1 km $s^{-1}$). The actual speeds of the boundaries between the various impact outcome regimes (Rebound, Sticking, and Cratering) depend on the projectile and target materials involved and are not necessarily sharp, but can involve a gradual transition from one regime to another (e.g., see Burke & Continetti, 2024, or Burchell & Wozniakiewicz, 2024). Furthermore, at some higher speed the projectile starts to fragment, then melt and finally vaporize (again with a gradual transition between regimes). Also, in the cratering regime, the crater shape itself evolves, from a shallow depression (low speed) to the fully formed "classic" impact crater with raised lips (high speed, see Figure 6a) characteristic of the strength dominated hypervelocity impact in a ductile medium (e.g., see fig. 1 in Bernhard & Hörz, 1995, fig. 2 in Wozniakiewicz et al., 2019, or fig. 2 in Fisher et al., 2021). Key here is that the cratering regime starts at around a km $s^{-1}$, that is, at the minimum sampling speeds for Io missions, and by some 5 km $s^{-1}$, the full classic hypervelocity impact crater is obtained in a typical ductile target. In more brittle materials, the initial central crater is surrounded by a wider spallation zone (Figure 6b) formed later in the impact process (e.g., see Burchell & Grey, 2001; Taylor et al., 1999).

TABLE 5. General schemes for appearance of peaks in impact mass spectra reported in literature.

| Fe on Rh (Ratcliff, Reber, et al., 1997) | Aluminosilicate clay on Rh (Goldsworthy et al., 2003) | Aromatic organics (polypyrrole and polystyrene latex) on Rh (Goldsworthy et al., 2003) | Aliphatic organics (Burchell and Armes, 2011) | Organic doped ices (Burke et al., 2023) | Horányi et al. (2019) |
|---|---|---|---|---|---|
| >1.5 km $s^{-1}$: N and K observed | <5 km $s^{-1}$: No data | <3 km $s^{-1}$: No data | <4.4 km $s^{-1}$: No data | <2 km $s^{-1}$: No impact ionization | 1–3 km $s^{-1}$: Can distinguish between rocky, organic, metallic |
| 15–20 km $s^{-1}$: Fe, Rh appear | 5–10 km $s^{-1}$: Mostly peaks below 60 amu (including Al and peaks at 7 and 43/44 amu), with a few higher mass peaks at 72, 87 and 115 amu | 3–5 km $s^{-1}$: High mass organic compound (HMOC) peaks visible (>200 amu), regularly spaced, 12–14 amu, indicating underlying chemistry of bonds corresponding to $[CH_3(CH{=}CH)_n(CH_2)_mCH_2]^+$ with mass numbers (M) given by M = 26n + 14 m + 29; where n and m = 0, 1, 2 …, etc. A peak at 91 amu is also visible, assigned to the tropylium cation | 4–7 km $s^{-1}$: Many regularly spaced peaks with strong peaks at 41, 69, 115 reflecting scission points in the C-C and C-O bonds in the parent molecule. The tropylium cation was not observed | 3 km $s^{-1}$: Molecular ions dominate | 3–5 km $s^{-1}$: Low ionization potential species. Also, species in icy matrices can be identified |
| 20–25 km $s^{-1}$: 5× Fe, Rh yield compared with 15 km $s^{-1}$ | >10 km $s^{-1}$: Only peaks below 60 amu (including Al). No peak is present at 43/44 amu, and the peak at 7 amu is absent above 16 km $s^{-1}$ | 5–10 km $s^{-1}$: Intermediate mass peaks (stronger below 100, but visible up to 150 amu), regularly spaced, 12–14 amu, indicating underlying chemistry of bonds as above. The peak at 91 amu (assumed to be the tropylium caption) still appears but is less strong and not observed in all events | >7.6 km $s^{-1}$: No data available | 4 km $s^{-1}$: Fragmentation species increasingly observed | 5–10 km $s^{-1}$: Wide range of large molecular fragments |
| 25–30 km $s^{-1}$: 30× Fe, Rh yield compared with 15 km $s^{-1}$ | | 10–15 km $s^{-1}$: Intermediate mass peaks (stronger below 100, with some visible up to <150 amu) regularly spaced, 12–14 amu, indicating underlying chemistry of bonds. The peak at 91 amu is no longer seen | | | 10–15 km $s^{-1}$: Fewer high mass peaks, more elemental peaks appear |
| 30+ km $s^{-1}$: 200× Fe, Rh yield compared with 15 km $s^{-1}$ | | 15–17 km $s^{-1}$: Intermediate mass peaks (some visible 50–100 amu, with few above 100 amu) regularly spaced, 12–14 amu, indicating underlying chemistry of bonds<br>20+ km $s^{-1}$: Only mass peaks <60 amu visible | | | 15–20 km $s^{-1}$: Elemental mass peaks, simpler spectra |

*Note*: The target peak is excluded from the discussion as it is usually present once a speed threshold is passed (Table 4), although it often broadens in width as speed then increases.

The next crucial observation is that the amount of impactor material that is retained at the impact site is also speed dependent (e.g., see discussion and fig. 2 in Wozniakiewicz et al., 2018). At around 1 km $s^{-1}$, broken, fragmented impactor is often found at the impact site. By 2 or 3 km $s^{-1}$, this relatively unprocessed material is replaced by increasing amounts of melt. At 5 km $s^{-1}$, melt dominates, and its location in the crater moves from the bottom of the crater up the crater walls. It is assumed that by 10 km $s^{-1}$, melted residue is minimized and the majority of the impactor has vaporized. When vaporization initially occurs, material may redeposit around the crater, but, as impact speed increases, it is assumed the vaporized material will have increasingly left the impact site and its environs. However, we note that as with impact outcome, the fate of the impactor (i.e., the exact manner and degree of impactor preservation observed) also depends on the combination of projectile and target materials as well as impact speed. Critically, the speed regimes discussed above cross the speed ranges proposed for Jovian Bound Orbit type sampling missions at Io. This is revisited later when shock pressures are discussed.

One difficulty that thus arises with the analysis of projectile residues after impact is the high degree of alteration during capture. The material is often highly processed, having at least partially melted. There can also be loss, or preferential loss, of different components, and different types of materials suffer losses at different impact speeds. Indeed, even if all components are retained there can be a loss of structural information (i.e., the bonding). This is not always the case; for example, it has been shown that some minerals (olivine, rhodonite, enstatite, diopside and wollastonite) impacting aluminum at 6 km $s^{-1}$ can retain their characteristic Raman spectra (indicative of structure), whereas lizardite (a phyllosilicate) does not (Burchell, Foster, et al., 2008).

There is also evidence for at least some mineralic impactor material surviving intact at 6 km $s^{-1}$, that is, it is the original crystallinity that is retained after capture, and the observed Raman spectra (i.e., structure) are not the result of recrystallization of the melted residue after cooling (Wozniakiewicz, Ishii, et al., 2012; Wozniakiewicz, Kearsley, et al. 2012). The impact-related shock pressures (see Peak Shock Pressures Section) experienced by the residues may, however, leave a strain-related shift in the observed Raman spectra. This can have consequences if detailed analysis is then performed. For example, the characteristic twin-peak pair in the Raman spectra of olivine at 820 and 850 $cm^{-1}$, can normally be used not just to flag the presence of olivine in a sample, but also its Mg:Fe ratio (i.e., fosterite versus fayalite, see Kuebler et al., 2006). It has been shown, however, that, even though the characteristic peaks for olivine can still be found in residues after capture in aluminum foil, there are subtle shock-related shifts in the peak positions, which, unless corrected for, alter the apparent Mg:Fe ratio (Foster et al., 2013; Harriss & Burchell, 2016). Shock-induced effects are also reported in the spectra of experimentally shocked basalts (Johnson et al., 2020). This would need to be allowed for in any detailed analysis.

It should be noted, however, that the best metal surfaces for capture are prepared for that purpose in advance, being uniform in composition (i.e., lack inclusions which may complicate compositional analysis) and smooth (preferably flat, to aid in crater recognition). This was not quite the case for the metal foils used on the Stardust flyby/sample-return mission to comet 81P/Wild 2, which suffered from deficiencies in both regards (e.g., see Kearsley et al., 2008; Leitner et al., 2008) because their primary purpose was to hold in place the aerogel samples used in that mission (Tsou et al., 2003). Nevertheless, the Stardust foils did provide extensive impact crater data, showing how powerful metal surfaces can be for sample return (e.g., Hörz et al., 2006).

Despite these caveats, the simplicity of use means that many missions have flown using metal surfaces (thick or thin) to obtain impactor information. These include: free flying satellites in Low Earth Orbit LEO (e.g., Solar Max, Laurance & Brownlee, 1986, the Long Duration Exposure Facility LDEF, Levine, 1993; Love & Brownlee, 1993, the European Retrievable Carrier EuReCa, Gardner et al., 1996, Yano et al., 1996); on the outside of Mir (Mandeville & Bariteau, 2001; Shrine et al., 1997); as well as missions further afield, such as Genesis (which sampled solar wind, see Burnett et al., 2003) and the Stardust mission which visited comet 81P/Wild-2 (Hörz et al., 2006).

### *Solar Cells*

Solar cells, arranged in solar panels to power spacecraft, have provided several opportunities to study impactor residues, for example, solar panels retrieved in Hubble Space Telescope (HST) service missions in 1993 (Graham, McBride, et al., 2001), and again in 2003 (Moussi et al., 2005), as well as from EuReCa in 1993 (Drolshagen et al., 1996) and Mir in 1997 (Mandeville & Bariteau, 2001). The key difference to impacts on thick metals is that the solar cells are not ductile, but brittle. Consequently, the solar cells and panels spall and fracture under impact, and larger impacts can lead to solar cell penetration and even panel fragmentation (e.g., see Olivieri Lorenzo et al., 2024). The resulting impact features are therefore complex, with a central pit (or hole) surrounded by a wider, shallow spall zone (see Figure 6b). Furthermore, the multilayered composition of solar cells makes unique identification of the impactor composition difficult, for example, see Kearsley, Drolshagen, et al. (2005); Kearsley et al. (2024).

Unfortunately, in a sample-return mission, the solar panels are not always subsequently stowed for retrieval even from LEO, for example, the solar panels on the Space Flyer Unit were not returned with the rest of the spacecraft (Yano et al., 1997). Indeed, for missions returning from deep space, the solar panels are not likely to be stowed inside the capsule that undertakes the Earth re-entry (e.g., Genesis and Stardust). Therefore, while some encounter science is possible (e.g., camera observations of the solar panel surface before and after encounter to directly observe larger impact craters, loss of power indicating degree of surface area damage and hence incident flux), detailed use in sample-return missions is limited.

### *Silicon and Germanium Wafers*

The use of ultrapure wafers of silicon (Figure 6f) or germanium as capture medium improves upon some of the difficulties presented by solar cells. The materials are pure, so detailed compositional analysis of the impactor residues is possible, and they can be readily mounted directly on the body of a spacecraft (e.g., as with LDEF, see Simon et al., 1991) or in a dedicated sample collector, so they will be stowed for Earth re-entry at mission end. Such wafers were used by the Genesis mission to collect solar wind (Burnett et al., 2003; Clark, 2001), where the use of ultrahigh purity media (including float-zone silicon and germanium) was essential for the high precision isotope analysis planned on return (Jurewicz et al., 2003; Meshik et al., 2007).

A discussion of the cratering process in silicon is given in Taylor et al. (2001), and laboratory tests of impacts onto silicon show that capture is possible (e.g., see fig. 7 in Graham, Kearsley, et al., 2001). However, this is impactor size and speed dependent. For example, particles in the size range <1 to 50 μm, and speeds 5–72 km $s^{-1}$, show a variety of results; at a few km $s^{-1}$, almost whole grains were found in the silicon for impacts by 1 μm particles, but in the 38–51 μm size range impact spallation had completely removed any macroscopic impactor residue (Graham et al., 2004). Clearly, understanding this size-dependent phenomenon is important when selecting capture media, as is any impact speed dependence (e.g., see Price et al., 2014, where impacts onto thin wafers are reported at speeds up to 4.1 km $s^{-1}$).

As well as the issue of collecting the impactor residue, the response of the wafers themselves to impact has to be considered. The wafers are thin and brittle. Thus, as well as spallation, there can be cracking in the wafers and this can lead to them breaking apart (dependent not just on the size and speed of the impactor, but also on the wafer fabrication method and crystal orientation, Chen et al., 2000).

### *Capture Cells*

One method of capturing impactors in a way which maximizes retention of impactor residue is to use a capture cell. This applies the long established principle of a thin front layer, followed by a gap and at least one or several more thin layers (and possibly a solid rear layer to capture any fully penetrating material). The impactor penetrates the front layer, possibly being disrupted in the process. Any disrupted material then spreads out as it proceeds to the next layer where it is hopefully captured. This process can be repeated across several subsequent layers. Even if the impactor passes through a layer (relatively) intact, it can still leave residue (from its surface) in the rim of the hole in the thin film as it passes through (e.g., see fig. 6 in Kearsley, Graham, et al., 2005). Capture cells can be specifically constructed for this purpose (e.g., McDonnell et al., 1984), or opportunistic use can be made of multilayered materials, such as multilayer insulation blankets, which effectively act as capture cells (e.g., Graham et al., 2003).

An early example of deployment in space of a capture cell was on the third space shuttle mission (STS-3 in 1982, see McDonnell et al., 1984). Capture cells have since been flown on a variety of missions in LEO, such as LDEF (e.g., Fitzgerald & Yano, 1995), EuReCa (e.g., Gardner et al., 1996; Yano et al., 1996), the Space Flyer Unit (where the multilayer insulation acted as a capture cell, Yano et al., 1997; Kearsley & Graham, 2004), etc., and have also been mounted on the exterior of both Mir (e.g., Shrine et al., 1997) and the International Space Station (ISS, e.g., Yamagishi et al., 2021). Improved designs are regularly suggested for future missions (e.g., Dignam et al., 2022; Kearsley, Graham, et al., 2005; Wozniakiewicz et al., 2019).

### *Aerogel*

As indicated above, even if residues are found after impacts on solid surfaces or in capture cells, there can be a high degree of impact processing, and this can vary with impactor composition. An improved method of capturing nearly intact material at high speeds has thus long been desired. In the 1980s and 1990s, various low-density materials, such as polymer foams, including polystyrene (e.g., Anderson & Ahrens, 1994; Maag & Linder, 1992; Tsou et al., 1984), were thus tried as capture media. The most successful low-density capture media, however, was $SiO_2$ aerogel (see Burchell, Graham, & Kearsley, 2006, for a review). As well as $SiO_2$ aerogel, other types of aerogel have also been suggested for use in space as dust collectors, including alumina, tantala and zirconia aerogels (e.g., see Jones & Flynn, 2006), zeolite-loaded aerogel aerogels (e.g., Petkov et al., 2019) and calorimetric aerogel (e.g., Domínguez et al., 2003).

Aerogel is a highly porous (open pore), solid material with typical densities for space use as low as 10–100 kg $m^{-3}$, and has a pore size of some 40–80 nm (e.g., see Burchell, Cole, & McDonnell, 1998). In such media, the impactor leaves an entrance hole in the front surface and then tunnels in, decelerating as it does so, and is found either at the end of the track (long thin, so-called carrot shaped tracks, e.g., Figure 6e), or as fragments lining the track walls, particularly in the cases of more bulbous cavities made when loosely bound material disperses during the impact capture process (see Burchell, Fairey, et al., 2008 and Trigo-Rodríguez et al., 2008 for detailed discussions). Aerogel can operate successfully as a capture medium over a wide temperature range, with laboratory studies reporting use from 175 to 763 K, although there is some alteration to the resulting track lengths and entrance hole sizes as target temperatures increase above some from 500 to 600 K (Burchell, Fairey, et al., 2009).

The capture process for particles in aerogel depends on the particle strength. For cohesive particles, it has been shown that track length, for example, can be well modeled using hydrodynamic forces (proportional to $v^2$) at high speed (km $s^{-1}$), and then at low speed (e.g., 200 m $s^{-1}$) the particles decelerate as a result of overcoming the aerogel crushing strength (see Kadono et al., 2012; Niimi et al., 2011). Weaker and volatile-rich particles produce bulbous cavities in aerogel, and the initial cavity formation can be modeled using thermodynamic processes, with the final cavity growth limited by the crushing strength of the aerogel (e.g., see Trigo-Rodríguez et al., 2008). The measured properties of the aerogel tracks combined with captured grain sizes can be used to infer pre-impact particle sizes (e.g., Burchell, Fairey, et al., 2008) and densities (e.g., Niimi et al., 2012).

Since the direction inferred from track length in aerogel corresponds to the impact direction to a high degree (e.g., see Figure 6e), it can be used to determine the direction of the impactor if the orientation of the aerogel at the time of impact is known, and thus to infer the likely origin. For example, Burchell, Thomson, and Yano (1998) determined a likely micrometeoroid origin with a retrograde trajectory for a particle captured in aerogel by the EuReCa mission, and Burchell et al. (2012) showed how to separate contaminants captured in aerogel in the Stardust interstellar collector arising from secondary ejecta from nearby impacts on the host spacecraft structure.

The material captured in aerogel can be studied in situ, for example, via Raman spectroscopy for both minerals (Burchell et al., 2001; Burchell, Mann, et al., 2006) and organics (Burchell et al., 2004), or via mass spectroscopy (Jones et al., 2015). Captured material can also be extracted for more detailed analysis (Burchell, Graham, & Kearsley, 2006; Westphal et al., 2004). Once extracted, a wide range of analysis techniques can be applied. If the analysis is performed on a spacecraft, it will, however, be limited by difficulties of extraction and the available power and mass budgets, as well as limited instrument complexity. In contrast, a sample returned to Earth can undergo any suitable analysis for small grain materials (e.g., see Zolensky et al., 2000). Bulk analysis of aerogel looking for more diffuse captured materials is also possible, for example, aerogel exposed during the flyby of comet Wild-2 was examined for evidence of glycine (Glavin et al., 2008) and also underwent helium and neon isotope analysis (Palma et al., 2019). Despite the presence of contaminants from manufacture and handling (e.g., see Tsou et al., 2003), a high degree of sensitivity is possible when analyzing aerogels. For example, Tabata et al. (2014) manufactured aerogels in a clean-room environment and which were then used on the Tanpopo experiment aboard the ISS. These aerogels should have very low levels of elemental impurities and can be used, like the Genesis collectors, to analyze the impactor and substrate together in a bulk analysis. Similarly, Jones et al. (2015) showed it was possible, after capture in aerogel, to identify organics, such as polycyclic hydrocarbons present as minor components in impacting particles.

Thus far, capture in aerogel has been associated with sample return rather than in situ analysis. A wide variety of samples have been space-exposed and returned. These include samples on STS flights 41B, 41D, 42, 47, 57, 60, 61D, 68, 69, 71 and 72 (Maag & Linder, 1992; Tsou, 1995), on the exterior of Mir (e.g., Hörz et al., 2000; Shrine et al., 1997; Westphal et al., 1998), on the EuReCa spacecraft (Burchell, Thomson, & Yano, 1998), on the outside of the ISS (e.g., the Tanpopo experiment, see Yamagishi et al., 2021), and from the flyby of comet Wild-2 by the Stardust spacecraft. A summary of the key initial Stardust results is in Brownlee et al. (2006), with details of the aerogel tracks in Hörz et al. (2006), discussion of the captured grain mineralogy in Zolensky et al. (2006), isotope analysis in McKeegan et al. (2006), and there are more detailed later reviews, such as Brownlee (2014) and Ogliore (2023). As well as visiting comet Wild-2, the Stardust mission also exposed aerogel while in its cruise phase to the interstellar dust stream, and obtained several candidate interstellar impacts in both aerogel and on exposed metal foils (Westphal et al., 2014).

### *Metal Foams*

An alternative capture media to aerogels (which are brittle and may break apart during impacts by larger particles) are metal foams. These have open pore structures with metal ligaments (Figure 6c,d). On impact, an incident particle effectively undergoes multiple shocks, fragmenting and producing a cloud of debris which is captured in the foam (assuming it does not fully

TABLE 6. Coefficients for the planar impact approximation, where shock wave speed U and particle speed u are related by the form U = c + Su.

| Material | c (m $s^{-1}$) | S | Density (kg $m^{-3}$) | References |
|---|---|---|---|---|
| Aerogel | 1000(0.947 + 1.78ρ) | 1.201 + 0.824ρ | Varied | Anderson (1998) |
| Aluminum | 5300 | 1.37 | 2750 | Melosh (2013) |
| Basalt | 2600 | 1.62 | 2860 | Melosh (2013) |
| Germanium | 1980 | 1.63 | 5328 | Ahrens and Johnson (1995) |
| Glass (soda-lime) | 3960 | 0.57 | 2307 | Ahrens and Johnson (1995) |
| Gold | 3080 | 1.546 | 19,263 | Ahrens and Johnson (1995) |
| Ice | 1317 | 1.526 | 915 | Melosh (2013) |
| Indium | 5480 | 0.47 | 7281 | Ahrens and Johnson (1995) |
| Olivine | 6000 | 0.88 | 3246 | Ahrens and Johnson (1995) |
| Rhodium | 4790 | 1.38 | 2330 | Marsh (1980) |
| Silicon (110) | 9210 | 0.57 | 2330 | Strickson and Artacho (2016) |

*Note*: For aerogel, these coefficients depend on the given formula where the density $\rho$ is in units of g $cc^{-1}$.

penetrate). Typical descriptions of the response of such foams to hypervelocity impact are given in, for example, Destefanis et al. (2006); Ryan and Christiansen (2013, 2015); Cherniaev (2021); Tang et al. (2024).

Aluminum is a typical metal which can be readily foamed, resulting in a density 8% of that of the original bulk material, and with, depending on production method, 10 or 20 pores per 2.54 cm (usually given as Pores Per Inch, PPI) and metal ligaments some 10%–20% of the pore size. Pore diameters can be as small as a few 10s of microns, but on average are typically some 0.2–5 mm (again depending on production method). For example, a typical Al foam (Al6061-T6, with 8% of bulk density and 10 PPI) is described by Ryan and Christiansen (2015), as possessing pores of typically 2.33 mm diameter and ligament widths of 0.382 mm. Other metals such as copper, titanium, stainless steel, silver, etc., as well as ceramics, such as silicon carbide, can also be used to produce foams.

The foams are mostly intended for shielding spacecraft against impact damage and are effective at containing the disrupted impactor (if thick enough). By contrast, here the captured material itself is of interest. It might be in the form of discrete fragments or as material lining the walls of the pores where, for example, it can have recondensed from a vapor phase. Extracting it for individual fragment analysis would be difficult, but the foams can be cut to expose the pore surfaces along an impact track, allowing point analyses to be performed. Alternatively, the foams could be dissolved and a bulk analysis carried out. One point to note is that unlike the cases where foams are used for shielding purposes, here there is no need for a front plate to contain the foam and act as an initial disruptor for the impactor.

## PEAK SHOCK PRESSURES

### Planar Impact Approximation

In impact processes at the macroscopic scale, the events can be characterized by the peak shock pressure. This is related to the various wave speeds in the materials involved using the shock Hugoniot relations for those materials (for a fuller discussion, see Melosh, 2013). The peak shock pressure generated in an impact at normal incidence and at several km $s^{-1}$ can be estimated using the planar impact approximation (PIA), and is a function of the properties of both the impactor and target, as well as the impact speed, for example, Melosh (2013). The PIA needs linear shock wave data for the materials involved, of the form U = c + Su, where U and u are the shock wave and particle speeds, respectively, and c and S are material-dependent coefficients usually found from experiments (values used here are listed in Table 6). Note that if SI units are used for the speeds, c has units of m $s^{-1}$, while S is dimensionless.

The impactors in the sample collection at Io will be the discrete particles of volcanic debris. For simplicity, we assume that they are solid basalt (i.e., no porosity), and accordingly, in calculations we use basalt as the projectile as a proxy for particles captured in the volcanic plumes at Io. Basalt is readily available for test programs and has already been used as a projectile in various experimental studies, such as Schultz and Gault (1990a), and Wickham-Eade et al. (2018). It should be noted, however, that basalt is a complex material, containing many oxide components in different ratios depending on the source of the basalt; this represents an average behavior. In Table 6, the c and S coefficients for basalt are taken from Melosh (2013), however, that these are based upon older data stretching back to the 1960s. More recent work studying the shock Hugoniot of basalt includes that of

Nakazawa et al. (1997), who also provided values for c and S (1.5 and 3000 m $s^{-1}$, respectively, with an average basalt density of 2700 kg $m^{-3}$), as did Sekine et al. (2008) (1.3 and 3500 m $s^{-1}$, respectively, with basalt density of 2700 kg $m^{-3}$). As a sensitivity test, the peak pressure in the PIA was found for basalt impacting aluminum for all three sets of c and S values (Melosh, 2013; Nakazawa et al., 1997; Sekine et al., 2008). For impacts at 5 km $s^{-1}$, the pressures varied by 2.7%, rising to 6.7% at 10 km $s^{-1}$ (with those based on Sekine et al., 2008, the lowest, and those based on Melosh, 2013, the largest). In Nakazawa et al. (1997) and Sekine et al. (2008), similar basalt was used, and while its density was 2700 kg $m^{-3}$, it had 4%–7.5% porosity, giving a zero porosity density of 2875 kg $m^{-3}$ on average, similar to the value suggested by Melosh (2013). Repeating the sensitivity analysis using a density of 2875 kg $m^{-3}$ for Nakazawa et al. (1997) and Sekine et al. (2008)) produces peak pressures which agree with those based on Melosh (2013), to within 0.7% at 5 km $s^{-1}$ and 3% at 10 km $s^{-1}$. Here, we therefore use the c, S, and density values of Melosh (2013), in all calculations, but note this uncertainty. For larger scale hydrocode simulations, a strength model and equation of state for basalt was developed in the ANEOS formalism by Pierazzo et al. (2005), and has since been developed further by Sato et al. (2021).

Next, a target has to be decided. A range of collector materials has been discussed above, and various typical examples are given in Table 6. Aluminum, gold, and indium are all used as typical metal collector media. Germanium and silicon are typical wafer materials. Glass is used as a proxy for solar cell impacts, since there is typically a cover glass on the front face of the solar cell. Here, we use soda-lime glass as an example, but a variety of glass materials are used in practice. Aerogel does not have a single value for c and S, as these depend on the density of the aerogel. Thus in Table 6, the formula of Anderson (1998) is given, and values are obtained for different aerogel densities. Here, three densities were chosen as examples: 10, 35, and 100 kg $m^{-3}$, typical, respectively, of use in the Tanpopo mission on the ISS in LEO (Yamagishi et al., 2021), the Stardust mission to comet Wild-2 (Burchell, Fairey, et al., 2008), and a higher value similar to those commonly used in laboratory experiments (e.g., Burchell et al., 2001; Brotherton et al., 2024).

Finally, we use ice in calculations to show the difference in peak pressures for impacts by icy particles instead of basalt to show what would happen if a mission sampled material ejected from an icy body, such as Europa rather than from Io (it is common for Jovian missions to fly past more than one satellite).

The encounter speed is mostly set by the speed of the spacecraft. This is because the particles emitted in a volcanic plume are essentially at ballistic speeds (they will slow as they rise in altitude), which are typically limited to less than 0.5 km $s^{-1}$ (e.g., see Lorenz, 2015, for a discussion). The actual impact speed of a volcanic grain on a spacecraft is thus dominated by the spacecraft speed during the encounter, as given in Table 2.

## Calculated Peak Pressures

### *NonPorous Media*

Given the projectile, target, and speed, the peak impact pressures calculated from the PIA are shown in Figure 7. For impacts on nonporous targets (Figure 7a), at an encounter speed of 7–9 km $s^{-1}$ (as suggested for a Prometheus style mission), the peak pressures are in the range of some 60–267 GPa, depending on collector type and exact impact speed. By contrast, at 17–19 km $s^{-1}$, for an IVO style mission (Adams et al., 2012), peak pressures range from 242 to 1020 GPa, that is, a factor of 4 times greater.

There are issues with using the PIA at high shock speeds and associated peak shock pressures. The use of a linear shock wave relationship is not necessarily appropriate as shock speeds increase beyond the range where experimental data have been obtained. Recent modeling, however, suggests that in metals, for example, it is appropriate in cases up to pressures of 200 GPa (typical of the range in which experimental data exists), and that a higher order polynomial form of the wave speed relationship (rather than a linear one) only significantly improves the predictions above 800–1000 GPa (Zhao et al., 2025). Thus, the predictions here should be considered more reliable at low speed (less than 10 km $s^{-1}$) and as indicative of behavior at 17–19 km $s^{-1}$, but not extrapolated to even higher speeds.

### *Aerogel*

The peak pressures in aerogel (Figure 7b) are much less than in normal density solids. In low-density aerogel (up to 100 kg $m^{-3}$) at 7–9 km $s^{-1}$, peak pressures range from 0.6 to 9.5 GPa and from 3.5 to 38 GPa at 17–19 km $s^{-1}$. There are, however, issues with capture in aerogel at the higher speeds and shock pressures. For example, it has been suggested that track length and the fraction of impactor collected at the end of the track start to fall as speeds increase above a threshold which depends on aerogel density (Burchell et al., 2001). In that paper, the speed at which this effect takes over was, for 106 μm diameter soda-lime glass projectiles, inversely correlated with aerogel density and was estimated as being some 7 km $s^{-1}$ at 25 kg $m^{-3}$, falling to 5.5 km $s^{-1}$ at 96 kg $m^{-3}$. For example, projectiles impacting the 96 kg $m^{-3}$ density aerogel had already lost up to 20% of their diameter during capture at 6 km $s^{-1}$.

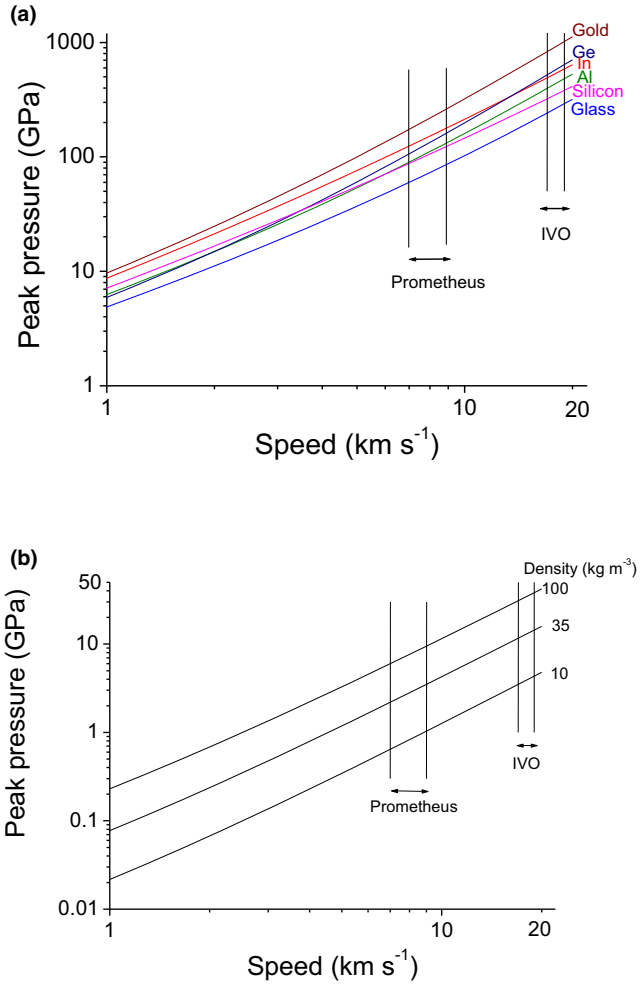


FIGURE 7. Peak impact pressures calculated from the planar impact approximation for basalt impacting (a) nonporous targets and (b) aerogels of various densities. The encounter speed ranges for proposed Prometheus and Io Volcano Observer (IVO) missions to Io are shown. (Color figure can be viewed at wileyonlinelibrary.com)

There is also evidence, from soda-lime glass particles (103 μm diameter) captured in aerogel, that not only does mechanical damage of the impactor (including fracturing) start to occur as impact speed increases, but that surface heating is also occurring with molten wraps of aerogel adhering to the captured particles (Burchell, Fairey, et al., 2009). Larger stainless steel spheres (500 μm diameter) have been shown to undergo significant ablation when impacting even low-density aerogel (25 kg $m^{-3}$) at speeds as low as 3.1 km $s^{-1}$ (see fig. 16 in Burchell, Fairey, et al., 2009, where the leading hemisphere of the originally spherical impactor has become cone shaped as a result of capture in the aerogel, with some melted steel redeposited as a rim around the projectile's equator and the rest has been lost). Similarly, organic microparticles (polystyrene latex) initially 20 μm in diameter lose approximately 50% of their diameter (and hence some 84% of their mass) during impacts into aerogel (density 25–35 kg $m^{-3}$) at 6 km $s^{-1}$, with this loss being attributed to ablative heating (Burchell, Foster, et al., 2009).

Given the wide range of impact conditions in the various published work on capture in aerogel (i.e., different size projectiles, of varying compositions impacting different density aerogels at different speeds), a full picture of capture does not emerge from just one paper. Hence, it is not clear which effects are predominantly due to the ablative heating or which are due to the shock pressure. Nevertheless, it appears that even at low impact speeds (few km $s^{-1}$) on low-density aerogel (<100 kg $m^{-3}$) weak impactors break apart early in the impact, causing a wide bulbous cavity in the aerogel lined with small impactor fragments, whereas well consolidated grains penetrate relatively deeply into the aerogel with the majority of the impactor retained as a single, discrete particle at the end of a narrow track (Burchell, Fairey, et al., 2008). Particles with several loosely bound discrete components may cause tracks intermediate between these two types (see Burchell, Fairey, et al., 2008). However, critically for capture at Io, at higher speeds above 5 or 6 km $s^{-1}$, there is evidence that even well consolidated particles can fracture and that ablative heating becomes important (Burchell, Fairey, et al., 2009; Burchell, Foster, et al., 2009), reducing the mass captured in a discrete terminal grain at the end of a track. These effects are also dependent on aerogel density (with a higher speed threshold for their onset at lower aerogel densities) as well as particle size and composition.

Data for large particles (above micrometer size) impacting aerogel are lacking for speeds above 7 or 8 km $s^{-1}$. However, Postberg et al. (2014) report data on impacts of small 0.11–0.44 μm diameter poly(bis[4-vinylthiophenyl] sulfide) latex, orthopyroxene and olivine microparticles into 10 kg $m^{-3}$ density aerogel at 3–20 km $s^{-1}$. At the lower speeds they observe the classical "carrot" shaped tracks, but as speed increases, the tracks become relatively more bulbous, with less residue at their ends. Above 15 km $s^{-1}$, they do not observe any original, unaltered particulate matter at the end of tracks, just concentrations of what they considered to be recondensed projectile residue. Here, it should be noted that cometary dust particles captured in the Stardust aerogel at 6.1 km $s^{-1}$ included a size range down to the submicron scale. These submicron captured particles displayed only carrot shaped tracks, which were wider (track width/length in the range 0.1–0.4) than those from larger captured particles (track width/length <0.1), see figs. 18 and 20 in Burchell, Fairey, et al. (2008). This suggests that some of change in track shape is impactor size related and not just due to higher speed impacts.

As before, it is not totally clear if this difference in capture in aerogel at low and high speeds, which crudely

occurs around 10 km $s^{-1}$ (likely dependent on aerogel density), is due to the increasing shock at entry into the aerogel, or increased thermal ablation during the tunneling into the aerogel. However, either way there is a clear difference between the outcomes of capture in aerogel at speeds typical of a Prometheus style mission and an IVO type mission. In the former, aerogel will collect significant fractions of lightly shocked and relatively unaltered material at the end of tracks formed by well consolidated impactors or in the walls of more bulbous cavities for loosely bound impactors, whereas the latter mission type will yield highly altered and likely vaporized material, recondensed in the aerogel near the track wall or end.

### *Metal Foams*

Calculating the shock pressures for impacts on metal foams is different to an impact on an effectively semi-infinite solid medium or an ultralow-density media, such as aerogel. The issue concerns the pore size relative to the particle size. Unlike aerogel, the foams are typically macroporous (defined as pore sizes >50 nm, and here typically mm scale), not micro- (<2 nm) or meso- (2–50 nm) porous. So unless the particles are above this size, it is not clear what they impact at any given moment. A 3-D hydrocode simulation with full details of the foam structure and composition is required for a detailed study (e.g., Cherniaev, 2021; Ryan & Christiansen, 2015; Tang et al., 2024). Such studies typically assume the foam is the stuffing in a thin walled Whipple shield, and thus, the original impact occurs on a thin uniform plate of the wall material. The models show that the impact then proceeds in the foam itself as a series of random collisions with the metal ligaments in the foam, and while the resulting cavity develops roughly along the original line of flight of the impactor, asymmetries and "clumpiness" occur in the expanding cloud of disrupted projectile material and associated ejecta which accompanies it. It is assumed this is similar to what happens with a foam with no thin wall face plate, with the difference that the initial disruption of the projectile may occur at depth inside the foam when the first ligament material is encountered.

Regarding the peak shock pressure, some approximations can be made. If the projectile is significantly smaller than the ligament size, it may impact the middle of a ligament or an edge of a ligament. The first such impact may be on the front face plane of the foam, or in the interior, and the subsequent impacts then develop as a shower-like process, with a characteristic opening angle and depth depending on the impact speed and the properties of the foam and projectile. The peak shock pressure depends on the initial impact and on whether it is in the middle or edge of a ligament. If the pre-impact direction of flight is normal to the face of the foam, and the impact occurs on the middle of a ligament, then as regards the peak shock pressure, this can be taken as equal to that in an impact on a semi-infinite, nonporous material and the PIA can be applied. Then, depending on the ligament thickness compared with projectile size, the impact will penetrate the ligament and fragmented projectile and displaced ligament material will proceed into the interior. If the projectile impacts nearer the edge of the ligament, this penetration through the ligament will proceed more quickly (with less projectile disruption), becoming more akin to an oblique impact (e.g., Burchell & Mackay, 1998) with reduced peak shock pressure (see Pierazzo & Melosh, 2000b), and finally a ricochet-type impact (e.g., see Burchell et al., 2010, 2015; Schultz & Gault, 1990b), with a near intact projectile proceeding into the interior of the foam at high speed. This process then repeats until the resulting shower is fully captured. Key to this is the idea that the maximum pressure experienced in such impacts can be found from the PIA as before, and that this represents a maximum possible peak value, with the actual peak value in each shower being less than or equal to this value, with a distribution dictated by how the shower develops. A hydrocode simulation is required for a more detailed description of the shock history. Given the range of shocks that will occur in such impacts, there may be significant variation in the degree of impact processing of the captured material. A question then arises as to how to access the captured projectile material, and this is best addressed by laboratory experimental tests using, for example, two-stage light gas guns.

## Weak Impactors

Less well consolidated impactors with little internal strength are difficult to accelerate in laboratory experiments. Nevertheless, as already stated they are held to break apart on entry into aerogel even at speeds of a few km $s^{-1}$, producing very bulbous cavities lined with fragments of the original projectile (Burchell, Fairey, et al., 2008; Trigo-Rodríguez et al., 2008). The difference in the degree of processing of the individual fragments during capture at Prometheus and IVO impact speeds is likely similar to that for discrete, well consolidated grains.

## Outcomes for Basalt Versus Shock Pressure

Given that basalt is taken here as a proxy for the composition of grains in the Io plumes, the fate of basalt impactors as a function of impact shock pressure needs to be determined. This depends on the partitioning of energy during an impact, with the initial kinetic energy (KE) split spread into various categories (see Schultz & Gault, 1990a, for a discussion). These include: the KE of the rebounding particle or ejecta, the internal energy of the projectile (which can cause deformation, fragmentation and heating,

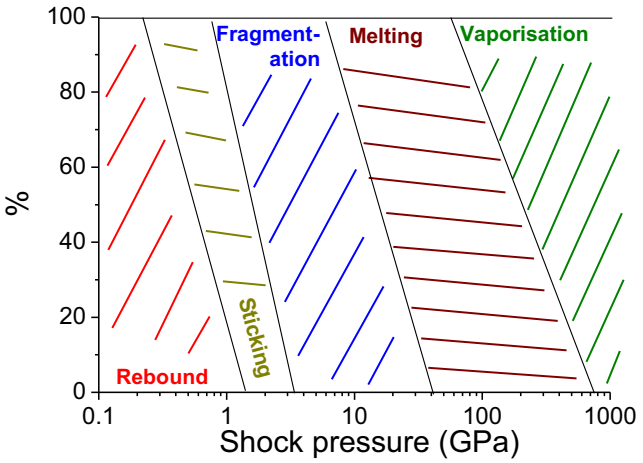


FIGURE 8. Fate of basalt impactor versus impact shock pressure (normal incidence). Also see Table 7. (Color figure can be viewed at wileyonlinelibrary.com)

the latter leading to melting and vaporization), the KE of any material set in motion in the target, and internal energy losses in the target. Here, we are concerned with the internal energy of the projectile.

We assume impact on a normal density medium of reasonable hardness such that penetration into the target has not occurred. As already stated, at low shock pressures rebound occurs. Then, depending on the target type, some form of indentation in the target surface starts to turn into the classic crater shape, accompanied by projectile fragmentation. As the shock pressure increases further, sufficient internal energy is available for melting and then vaporization. The thresholds for all these processes depend on projectile properties, such as strength, melting point and vaporization temperature. Furthermore, the boundaries between the impact outcomes (rebound, sticking, fragmentation, melting, and vaporization) are not sharp. These boundaries turn on for a small fraction of the impactors at one speed (shock pressure); this fraction then increases as speed (shock pressure) increases until the next step in the process occurs, and so on. This has been shown previously for impacts of ice onto metal targets versus impact speed (see fig. 6 in Miller et al., 2022, and fig. 7 in Burke & Continetti, 2024) and versus shock pressure (see fig. 7b in Burchell & Wozniakiewicz, 2024).

A scheme for the outcomes of impacts onto normal density targets of well consolidated basalt versus shock pressure is shown here in Figure 8 (and summarized in Table 7). Rebound is assumed to dominate at very low shock pressures. As pressure increases, the boundary between rebound and sticking is assumed to occur and the pressure thresholds may depend on target ductility as well as peak shock pressure. No exact data are available for basalt, but studies of impacts of other materials onto metals suggest sticking can occur between a few tenths of a

TABLE 7. Boundaries for impact outcome regimes for basalt versus peak shock pressure.

| Regime | Onset (GPa) | Complete (GPa) |
|---|---|---|
| Rebound | — | — |
| Sticking | 0.25 | 1.4 |
| Fragmentation | 1.4 | 3.5 |
| Melting | 10–15 | 40 |
| Vaporization | 65 | 750 |

*Note*: Rebound dominates at low shock pressures. See Figure 8 and main text for details.

GPa and a few GPa (e.g., see Fisher et al., 2021, for salt onto metal and Burchell & Wozniakiewicz, 2024 for ice onto metal). Wickham-Eade et al. (2018) reported intact capture of basalt impactors hitting water (considered equivalent to complete rebound or sticking) in impacts at 1.4 GPa. Then, above 1.4 GPa, fragmentation rapidly sets in. Wickham-Eade et al. (2018) gave the catastrophic disruption limit (where the mass of the largest fragment is ½ that of the original mass) for small basalt impactors as 1.5 GPa. At 1.6 GPa, the largest fragment mass was 20% of the original mass, and this had fallen below 1% by 1.95 GPa. Separately, it has also been shown that melting can start to occur in basalt under impact at 10 GPa (Ono et al., 2023), although earlier work suggests the onset of melting required at least 20 GPa. However, Ono et al. (2023) point out that while hydrocode simulations of the impact processes in basalt targets at 10 km $s^{-1}$ do not generate sufficient temperatures to cause melting, the simulations do not allow for localized increased energy densities (and hence temperatures) due, for example, to shear heating between minerals of different densities in the basalt. Based on laser irradiance experiments, it has been suggested that onset of melting of basalt in impacts does not occur until 70 GPa, and incipient vaporization at 270 GPa (Hamann et al., 2016). Note that in these melting and vaporization experiments, the basalt was the target rather than projectile, and the shock pressures were not directly measured, but were established by calculations which assumed thermal equilibrium, which may well not apply in such impacts. Nevertheless, the pressures quoted are taken as setting a scale.

These results for basalt can be compared with those for soda-lime glass impacting aluminum 1100, where Bernhard and Hörz (1995) reported that the glass projectile had started to become molten by 2.2 km $s^{-1}$ (15 GPa, calculated here using the PIA), and was almost fully molten by 5 km $s^{-1}$ (41 GPa). There were, however, still unmelted fragments detectable at 7 km $s^{-1}$ (65 GPa). The associated shock pressures are similar to those listed here for basalt. Such observations would explain why Raman studies on minerals impacting aluminum find recognizable Raman spectra at speeds up to at least 6 km

$s^{-1}$ (Burchell, Foster, et al., 2008), and why these are not considered to be from recrystalised melt (Wozniakiewicz, Kearsley, et al., 2012).

There are strain rate issues with using the PIA for impacts by submicron sized particles, where strain hardening may occur due to the ultrahigh strain rate arising from the small projectile size, and it is not clear how this will change the peak pressures generated in impacts (Price et al., 2013). However, with this caveat, the PIA can be used to set a scale for impacts at this size. Experiments for TOF mass spectroscopy using orthopyroxene (often found in basalts) impacting rhodium (Fiege et al., 2014) show that most diagnostic species are present in mass spectra for 10% of impacts at between 4 and 7 km $s^{-1}$ (67.5–164 GPa), in 50% of impacts at between 5 and 10 km $s^{-1}$ (5–296 GPa) and in over 90% of impacts at between 10 and 17 km $s^{-1}$ (296–746 GPa). These values help to set the upper boundaries for melting and vaporization of basalt in impacts (Figure 8 and Table 7).

It should also be noted that the location of the boundaries of the "Sticking" region in Figure 8 is in essence, a guestimate. Sticking has been observed in various previous experiments with other projectiles, such as salt (Fisher et al., 2021) and poly(methyl methacrylate) (New et al., 2020). It occurs typically in the regime when indentation in the target surface (and associated rebound) is starting to turn into cratering, but before projectile fragmentation occurs. This is what is shown in Figure 8, but a more correct estimate of the boundaries awaits a detailed study of basalt projectiles impacting a well-defined metal surface at various speeds, with associated shock pressure calculations.

### Reducing the Impact Peak Shock Pressure

As well as using a porous collection medium, another way to reduce the peak shock pressure in impacts is to have an inclined impact. In such impacts, it has previously been shown that peak shock pressures fall with $\sin\theta$, where $\theta$ is the angle of incidence measured from the plane of the target (Pierazzo & Melosh, 2000a, 2000b). As already stated, the angle of incidence between a plume particle and a passing spacecraft depends on the relative trajectories and, at Io, will mostly be dominated by the spacecraft motion. But the dust collector can also be inclined relative to the spacecraft's direction of motion, permitting a choice of impact angle, thus providing a way to reduce peak impact pressure.

There are some important caveats to the issue of inclined impacts. At shallow angles of incidence, increasing amounts of projectile material can be carried away from the impact site as ejecta. In addition, the impactor material retained in the impact crater is distributed preferentially in the uprange part of the crater and can show signs of lesser shock (Daly & Schultz, 2018). This is evident at incidences around 30° from the horizontal. Then, at shallower incidence, "impact decapitation" occurs, whereby the projectile shears during the initial impact, with the lower portion retained in the initial crater, and parts of the upper regions of the projectile continuing downstream, impacting beyond the original crater (Schultz & Gault, 1990b, also see fig. 2 in Burchell & Mackay, 1998, where secondary cratering appears downstream of the initial crater at 10° incidence from the horizontal). At very shallow angles (typically less than 10°), intact ricochet of the entire projectile at high speed can occur (e.g., Burchell et al., 2010, 2015; Gault & Wedekind, 1978; Schultz & Gault, 1990b). It was shown by Burchell et al. (2010) that the ricochet speed exceeds more than 95% of the incident speed for impact angles of less than 2°, with the outgoing angle slightly smaller than the incident angle. In that work, capture of the ricochet projectile at normal incidence on a subsequent surface produced impact craters very similar to those of direct impacts on such a surface, indicating that the ricochet projectile still undergoes an extreme shock when it hits a secondary surface. Thus, caution must be exercised in the employment of very shallow angles of impact for dust capture.

At low speeds and shock pressures, where rebound occurs anyway, inclined impacts could, however, be used to direct particles into the interior of a collector system. At higher pressures, where in normal incidence impact melt starts to occur, there is a separate problem, namely that the peak shock temperature has a different dependence on angle of incidence to that for pressure, and varies with $\sin^{1.5}\theta$ (Pierazzo & Melosh, 2000b). Hydrocode modeling suggests that the volume of melt that is produced in an impact seems to depend on crater volume, which in turn is angle of incidence dependent (Pierazzo & Melosh, 2000c). It has also been shown experimentally that in ductile materials at fixed impact energy, crater volume depends on $\sin\theta$ (e.g., Bryan & Pugh, 1962; Burchell et al., 1999), although Davison et al. (2011) suggest $\sin^{1.6}\theta$ is more appropriate. It should also be noted that, while at high speeds, shallow angle incidence may, via ricochet, help focus the incident impactor flux into a (smaller) collector area, as discussed above the final impact will still be at high speed and consequently high shock pressures.

It should be noted that this discussion applies to the transient crater produced in nonporous, ductile, or noncohesive materials. If the target were brittle, such as glass for example, different behavior may occur when the overall crater, including spallation is considered (e.g., Burchell & Grey, 2001). And for porous media such as aerogel, there is little difference between normal incidence and inclined impacts (although the shape of the entrance hole does change).

In the case of Io plume collection, an inclined collection can provide important information on volatile loss, mineral alteration, and isotope fractionation effects. Suppose the spacecraft speed is 7 km $s^{-1}$ with respect to Io's surface (i.e., a Prometheus-NF type mission), and the upward speed of the plume-entrained pyroclasts is 350 m $s^{-1}$. For the first sample collection exposure, let the collector normal vector be oriented parallel to the spacecraft's velocity vector. Then, for the second sample collection on a later orbit, the collector could be rotated 90 degrees so that the collector normal vector is oriented perpendicular to the spacecraft's velocity vector and parallel to the plume pyroclasts moving upward from Io's surface. On the first pass, the pyroclasts impact the surface at an angle atan(7000/350) = 87 degrees from the plane of the collector surface. On the second pass, the angle is atan(350/7000) = 3 degrees from the collector surface. The peak shock pressure is then reduced in the ratio sin(87)/sin(3), that is, a factor of 19. The corresponding ratio of shock temperatures between the "normal" and "grazing incidence" collections is: $\sin^{1.5}(87°)/\sin^{1.5}(3°)$, that is, a factor of 83 (Pierazzo & Melosh, 2000b). Therefore, the pyroclasts collected in the "grazing incidence" collection are captured with much less thermal modification than the "normal" collection.

There are problems with such inclined detector designs. For example, the effective surface area of the collector as seen by the plume is reduced. Thus, the amount of material collected in the "normal" divided by the amount of material in the "grazing incidence" collections is sin(87°)/sin(3°) = 19. Worse, as already stated, at extreme low angles of incidence of a few degrees, impactor ricochet can occur, with a significant fraction, and, at very shallow incidence, even all of the impactor material rebounding off the target and traveling away at high speed. This would have to be determined for a particular collector material, but a typical shallow impact angle which produces a well formed impact crater, and thus may retain a significant fraction of the impactor at the impact site, would likely be 10°–15° from the target surface (see Burchell & Mackay, 1998a, 1998b, for a discussion of critical shallow impact angles).

A sample-return mission design that collects material from the same plume twice using these two orientations has a number of advantages. The "grazing incidence" collection could be used to study trapped volatiles (like noble gases) and volatile coatings (as found on the lunar volcanic beads, e.g., Williams et al., 2025), the abundance and isotopic composition of more volatile species like sulfur and chlorine (de Kleer et al., 2024), and to search for intact magma chamber crystals and other phases that may not survive the high temperatures of the "normal" collection. The "normal" collection can be used to study the more refractory elements like chromium and tungsten, with sample concentrations high enough to allow for high-precision "bulk" isotope measurements (better than per-mil precision). A measurement of the isotopic composition over multiple systems spanning a range of volatility (say Ca, K, and Zn) on both the "grazing incidence" and "normal" collections will provide a measure of fractionation effects (changes in isotopic and elemental composition) due to capture. This double collection, and appropriate analysis of the returned sample, would minimize concerns related to the high-speed sample collection. A returned Io sample collected this way then becomes more similar to a small amount of fresh volcanic pyroclasts collected gently from Io's surface (a mission design that is impossible with today's technologies).

## Projectile Retention at Impact Site

While Figure 8 may be useful in terms of indicating the degree of impactor processing in an impact, it does not necessarily indicate the degree of projectile material retention at the impact site. For example, at low shock pressures, rebound occurs with little if any material left at the impact location. Then, as pressure increases and rebound stops, sticking implies a significant fraction of material is retained. The next step, fragmentation does not, however, imply that all the material is retained; it may be carried away from the impact site as ejecta (e.g., Burchell et al., 2012, show that kamacite projectile material can be found mixed with target material in the ejecta after an impact).

As impact speed increases further, projectile melt is then produced and found within the crater. However, for impacts of soda-lime glass on aluminum, Bernhard and Hörz (1995) noted that, while at 2.2 km $s^{-1}$ the projectile melt is located at the bottom of the floor, it begins to spread out at 2.5 km $s^{-1}$ (17 GPa), rising up the crater walls. The entire interior of the crater is then lined with melt at 3.5 km $s^{-1}$ (26 GPa). As the impact speed was raised further, increasingly large fractions of melt escaped between 5 and 7 km $s^{-1}$. They suggested that even modest increases in impact speed beyond this would see all the melt escape, but there is little or no data above 7 km $s^{-1}$. Separate studies of the retention of soda-lime glass residue in craters versus speed produce similar results, with melt layers some 90 nm thick from impact by a 1.6-μm diameter particle and 2 μm thick from a 440-μm diameter particle being reported for silicate impactors at 6 km $s^{-1}$, and the retained melt volume being estimated as some 50% of the original mass (Wozniakiewicz et al., 2018).

A separate issue is whether or not all components of a basalt are preserved equally. There is evidence that at 6 km $s^{-1}$, the constituent elements in basaltic glass are retained in equal proportions when averaged over a whole impact crater (see table 5 in Kearsley et al., 2007),

although this can be variable at discrete points inside a crater. A careful study of basalt impacts versus impact speed is thus required to quantify the degree of retention.

It should also be remembered that brittle targets will behave differently to ductile ones in terms of forming wide spall zones rather than simple bowl-shaped craters. Indeed, the spallation process may carry away much of the impactor material that might otherwise be retained in a crater (although counterexamples exist, see fig. 7 in Graham, Kearsley, et al., 2001, where an almost intact iron projectile is visible after impact on a silicon wafer).

Regarding retention, the use of porous media such as aerogel or foams is likely to be of significance. Following the earlier discussion, at low speed, impactor size-dependent effects (relative to pore size in the target) may influence rebound versus sticking, for example. Next, as speed increases, the strength of the impactor (strong and well consolidated or weak and porous) influences how it behaves when it penetrates the target, doing so as either a single particle or effectively breaking apart into multiple fragments. Then, even when impactors penetrate an underdense target, ablation of the impactor can occur as it tunnels into an aerogel target. Furthermore, any vaporized impactor material may recondense in the aerogel or metal foam, and thus still be retained (e.g., Ishii et al., 2008). Again, a detailed program of study of the behavior of basalt projectiles versus impact speed is to be encouraged for any particular underdense medium.

## CONCLUSIONS

To date, encounter speeds at Io have been in excess of 10 km $s^{-1}$. However, if macroscopic, semi-intact or relatively unprocessed material is to be collected for analysis at Io, then a low encounter speed is required, less than 10 km $s^{-1}$. This places constraints on the spacecraft flight trajectory. Orbits of Io itself (either circular or elliptical) permit low collection speeds (1–2.5 km $s^{-1}$), but such orbits are unlikely due to the radiation dose a spacecraft will accumulate in the vicinity of Io. However, encounter speeds below 10 km $s^{-1}$ can still be obtained (e.g., Ogliore et al., 2023), either for a Jovian Bound Orbit in which the Io encounter is prioritized (7 km $s^{-1}$) or via a single flyby on a heliocentric orbit with associated sample return to Earth (9 km $s^{-1}$).

At a given speed, the associated peak shock pressures experienced by the captured particle depend on the nature of the collector. For speeds from 1 to 20 km $s^{-1}$ the peak pressures in solid media are typically 5–100s of GPa, with lower pressures in underdense, porous media, such as aerogel (0.01–5 GPa). In the specific speed regime of 7–9 km $s^{-1}$, the shock pressures in solid, nonporous media range from 60 to 267 GPa, with 0.6–9.5 GPa in typical low-density aerogels. The result is that it is possible to collect significant proportions of mineralic impactors in a range of capture media. In solid, nonporous media, the captured material will likely be almost completely melted. However, in aerogel, relatively unprocessed impactor material will be obtained, either as a discrete grain at the end of a long, relatively narrow track for strong, well consolidated impactors, or as fragments lining a more bulbous cavity for weaker, less well consolidated material. Aerogel can also collect any volatile elements released during capture. In the latter case, the use of ultraclean aerogels would be important for high-precision composition studies.

The amount of material collected also critically depends on the incident flux. Models of the plumes indicate that pyroclasts are expected with mean sizes in the range 25–30 μm, and even up to 100 μm (e.g., Ogliore & Wilson, 2025). The number of such particles collected will depend on the plume density at the encounter altitude, as well as the number of passes through the plume. However, models suggest that even a single pass of a collector with exposed area of 0.1 $m^2$ (as in the NASA Stardust mission to comet Wild-2) could collect over 500 mg of material at 50 km altitude.

In a single mission, a suite of collector types would offer a range of surfaces as collection media, preserving impactor remnants with a range of capture induced alteration. A variety of science goals can thus be accommodated, with different collector media providing samples in an appropriate state for each. These samples would then be available for analysis either in situ or after sample return. If bulk processing of samples is all that is needed, collector media processing and sample extraction become relatively straightforward (e.g., by acid dissolution). If samples are embedded in aerogels, or as melt on the walls of craters, extraction can be difficult or it has to be analyzed in place. However, there are solutions. For example, soft metal foil collectors can have craters pressed out from the rear to bring their interiors back to the original surface plane where they may be more readily examined or extracted (Wozniakiewicz et al., 2018), and aerogel, being transparent, can be subject to optical and Raman analysis (e.g., Burchell et al., 2001, 2006; Foster et al., 2013). Nevertheless, the handling and analysis of captured materials is easier, and more efficient and effective in a sample-return mission, where the work can be done in the laboratory on Earth.

*Acknowledgments*—We thank the McDonnell Center for the Space Sciences at Washington University, St. Louis, and the Royal Society, London (IES\R2\232154), for funding. We also wish to thank the referees K. Kurosawa and R. Srama for their careful reading of the manuscript and comments thereon.

*Conflict of Interest*—The authors declare no conflict of interest.

*Data Availability Statement*—Data sharing is not applicable to this article as no data sets were generated or analyzed during the current study.

*Editorial Handling*—Dr. Gordon Osinski

## REFERENCES

Adams, E., Hibbard, K., Turtle, E., Reynolds, E., Anderson, B., Paranicas, C., Rogers, G., et al. 2012. Io Volcano Observer's (IVO) Integrated Approach to Optimizing System Design for Radiation Challenges IEEE Aerospace Conference, Big Sky, MT, USA, 1–13. https://doi.org/10.1109/AERO.2012.6187177.

Ahrens, T. J., and Johnson, M. L. 1995. Shock Wave Data for Rocks. In *AGU Reference Shelf 3: Rock Physics and Phase Relations, A Handbook of Physical Constants*, edited by T. J. Ahrens, 35–44. Washington, DC: American Geophysical Union.

Anderson, J. D., Null, G. W., and Wong, S. K. 1974. Gravitational Parameters of the Jupiter System from the Doppler Tracking of Pioneer 10. *Science* 183: 322–23. https://doi.org/10.1126/science.183.4122.322.

Anderson, W. W. 1998. Physics of Interplanetary Dust Collection With Aerogel. NASA Technical Report CR-1998–207766 https://ntrs.nasa.gov/citations/19980107921.

Anderson, W. W., and Ahrens, T. J. 1994. Physics of Interplanetary Dust Capture Via Impact into Organic Polymer Foams. *Journal of Geophysical Research* 99(E1): 2063–71. https://doi.org/10.1029/93JE03147.

Bagenal, F., and Dols, V. 2020. The Space Environment of Io and Europa. *Journal of Geophysical Research: Space Physics* 125: e2019JA027485. https://doi.org/10.1029/2019JA027485.

Bedford, D. K. 1971. Impact Ionization of Micro-Particles at Low Velocities. *Journal of Physics A: General Physics* 4: L14–L18. https://doi.org/10.1088/0305-4470/4/1/022.

Bernhard, R. P., and Hörz, F. 1995. Craters in Aluminum 1100 by Soda-Lime Glass Spheres at 1 to 7 km/s. *International Journal of Impact Engineering* 17: 69–80. https://doi.org/10.1016/0734-743X(95)99836-G.

Brotherton, E. E., Chan, D. H. H., Armes, S. P., Janani, R., Sammon, C., Wills, J. L., Tandy, J. D., et al. 2024. Synthesis of Phenanthrene/Pyrene Hybrid Microparticles: Useful Synthetic Mimics for Polycyclic Aromatic Hydrocarbon-Based Cosmic Dust. *Journal of the American Chemical Society* 146: 20802–13. https://doi.org/10.1021/jacs.4c04330.

Brownlee, D. E. 2014. The Stardust Mission: Analyzing Samples from the Edge of the Solar System. *Annual Review of Earth and Planetary Sciences* 42: 179–205. https://doi.org/10.1146/annurev-earth-050212-124203.

Brownlee, D. E., Tsou, P., Aléon, J., Alexander, C. M. O'D., Araki, T., Bajt, S., Baratta, G. A., et al. 2006. Comet Wild-2 under a Microscope. *Science* 314: 1711–16. https://doi.org/10.1126/science.1135840.

Bryan, G. M., and Pugh, E. M. 1962. Cratering of Lead by Oblique Impacts of Hypervelocity Steel Pellets. *Journal of Applied Physics* 33: 734–38.

Burchell, M. J., and Armes, S. P. 2011. Impact Ionization Spectra from Aliphatic PMMA Microparticles. *Rapid Communications in Mass Spectroscopy* 25: 543–550. https://doi.org/10.1002/rcm.4887.

Burchell, M. J., Cole, M. J., and McDonnell, J. A. M. 1998. Role of Particle Charge in Impact Ionization by Charged Microparticles. *Nuclear Instruments and Methods in Physics Research Section B* 143: 311–18. https://doi.org/10.1016/S0168-583X(98)00371-1.

Burchell, M. J., Cole, M. J., McDonnell, J. A. M., and Zarnecki, J. C. 1999. Hypervelocity Impact Studies Using the 2 MV Van de Graaff Dust Accelerator and Two Stage Light Gas Gun of the University of Kent at Canterbury. *Measurement Science and Technology* 10: 41–50. https://iopscience.iop.org/article/10.1088/0957-0233/10/1/011/pdf.

Burchell, M. J., Cole, M. J., Price, M. C., and Kearsley, A. T. 2012. Experimental Investigation of Impacts by Solar Cell Secondary Ejecta on Silica Aerogel and Aluminium Foil: Implications for the Stardust Interstellar Dust Collector. *Meteoritics & Planetary Science* 47: 671–683. https://doi.org/10.1111/j.1945-5100.2011.01294.x.

Burchell, M. J., Cole, M. J., Ramkisson, N. K., Wozniakiewicz, P. J., Price, M. C., and Foing, B. 2015. Smart-1 End of Life Shallow Regolith Impact Simulations. *Meteoritics & Planetary Science* 50: 1436–48. https://doi.org/10.1111/maps.12479.

Burchell, M. J., Cole, M. J., and Ratcliff, P. R. 1996. Light Flash and Ionization from Hypervelocity Impacts on Ice. *Icarus* 122: 359–365. https://doi.org/10.1006/icar.1996.0129.

Burchell, M. J., Creighton, J. A., Cole, M. J., Mann, J., and Kearsley, A. T. 2001. Capture of Particles in Hypervelocity Impacts in Aerogel. *Meteoritics & Planetary Science* 36: 209–221. https://doi.org/10.1111/j.1945-5100.2001.tb01865.x.

Burchell, M. J., Creighton, J. A., and Kearsley, A. T. 2004. Identification of Organic Particles Via Raman Techniques after Capture in Hypervelocity Impacts on Aerogel. *Journal of Raman Spectroscopy* 35: 249–253. https://doi.org/10.1002/jrs.1143.

Burchell, M. J., Fairey, S. A. J., Foster, N. J., and Cole, M. J. 2009. Hypervelocity Capture of Particles in Aerogel: Dependence on Aerogel Properties. *Planetary and Space Science* 57: 58–70. https://doi.org/10.1016/j.pss.2008.11.004.

Burchell, M. J., Fairey, S. A. J., Wozniakiewicz, P., Brownlee, D. E., Hörz, F., Kearsley, A. T., See, T. H., Westphal, A., Green, S. F., and Trigo-Rodríguez, J. M. 2008. Characteristics of Cometary Dust Tracks in Stardust Aerogel and Laboratory Calibrations. *Meteoritics & Planetary Science* 43: 23–40. https://doi.org/10.1111/j.1945-5100.2008.tb00608.x.

Burchell, M. J., Foster, N. J., Kearsley, A. T., and Creighton, J. A. 2008. Identification of Mineral Impactors in Hypervelocity Impact Craters in Aluminium by Raman Spectroscopy of Residues. *Meteoritics & Planetary Science* 43: 135–142. https://doi.org/10.1111/j.1945-5100.2008.tb00614.x.

Burchell, M. J., Foster, N. J., Ormond-Prout, J., Dupin, D., and Armes, S. P. 2009. Extent of Thermal Ablation Suffered by Model Organic Microparticles During Aerogel Capture at Hypervelocities. *Meteoritics & Planetary Science* 44: 1407–20. https://doi.org/10.1111/j.1945-5100.2009.tb01182.x.

Burchell, M. J., Graham, G., and Kearsley, A. 2006. Cosmic Dust Collection in Aerogel. *Annual Reviews of Earth and*

*Planetary Science* 34: 385–418. https://doi.org/10.1146/annurev.earth.34.031405.124939.

Burchell, M. J., and Grey, I. D. S. 2001. Oblique Hypervelocity Impacts on Thick Glass Targets. *Materials Science and Engineering A* 303: 134–141. https://doi.org/10.1016/S0921-5093(00)01847-5.

Burchell, M. J., and Mackay, N. G. 1998. Crater Ellipticity in Hypervelocity Impact on Metals. *Journal of Geophysical Research* 103: 22761–74. https://doi.org/10.1029/98JE02143.

Burchell, M. J., Mann, J., Creighton, J. A., Kearsley, A. T., Graham, G., and Franchi, I. A. 2006. Identification of Minerals and Meteoritic Materials Via Raman Techniques after Capture in Hypervelocity Impacts on Aerogel. *Meteoritics & Planetary Science* 41: 217–232.

Burchell, M. J., Robin-Williams, R., Foing, B. H., and the SMART-1 Impact Team. 2010. The SMART-1 Lunar Impact. *Icarus* 207: 28–38. https://doi.org/10.1016/j.icarus.2009.10.005.

Burchell, M. J., Thomson, R., and Yano, H. 1998. Capture of Hypervelocity Particles in Aerogel: In Ground Laboratory and Low Earth Orbit. *Planetary and Space Science* 47: 189–204. https://doi.org/10.1016/S0032-0633(98)00085-3.

Burchell, M. J., and Wozniakiewicz, P. J. 2024. Icy Ocean Worlds, Plumes and Tasting the Water. *Meteoritics & Planetary Science* 59: 1385–1406. https://doi.org/10.1111/maps.14152.

Burke, S. E., Auvil, Z. A., Hanold, K. A., and Continetti, R. E. 2023. Detection of Intact Amino Acids with a Hypervelocity Ice Grain Impact Mass Spectrometer. *Proceedings of the National Academy of Sciences of the United States of America* 120: e2313447120. https://doi.org/10.1073/pnas.2313447120.

Burke, S. E., and Continetti, R. E. 2024. Submicrometer Particle Impact Dynamics and Chemistry. *Annual Review of Physical Chemistry* 75: 67–88. https://doi.org/10.1146/annurev-physchem-083122-122157.

Burnett, D., Barraclough, B., Bennett, R., Burnett, D. S., Barraclough, B. L., Neugebauer, M., Oldham, L. P., et al. 2003. The Genesis Discovery Mission: Return of Solar Matter to Earth. *Space Science Reviews* 105: 509–534. https://doi.org/10.1023/A:1024425810605.

Chan, D. H., Millet, A., Fisher, C. R., Price, M. C., Burchell, M. J., and Armes, S. P. 2021. Synthesis and Characterization of Polypyrrole-Coated Anthracene Microparticles: A New Synthetic Mimic for Polyaromatic Hydrocarbon-Based Cosmic Dust. *ACS Applied Materials & Interfaces* 13: 3175–85. https://doi.org/10.1021/acsami.0c19758.

Chan, D. H. H., Wills, J. L., Tandy, J. D., Burchell, M. J., Wozniakiewicz, P. J., Alesbrook, L. S., and Armes, S. P. 2023. Synthesis of Autofluorescent Phenanthrene Microparticles Via Emulsification: A Useful Synthetic Mimic for Polycyclic Aromatic Hydrocarbon-Based Cosmic Dust. *ACS Applied Materials & Interfaces* 15: 54039–49. https://doi.org/10.1021/acsami.3c08585.

Chen, Q., Yao, D. J., Kim, C. J., and Carman, G. P. 2000. Investigating the Influence of Fabrication Process and Crystal Orientation on Shear Strength of Silicon Microcomponents. *Journal of Materials Science* 35: 5465–74. https://doi.org/10.1023/A:1004873029495.

Cherniaev, A. 2021. Modeling of Hypervelocity Impact on Open Cell Foam Core Sandwich Panels. *International Journal of Impact Engineering* 155: 103901. https://doi.org/10.1016/j.ijimpeng.2021.103901.

Clark, B. C. 2001. The Genesis Mission: Unifying Science and Engineering. *Acta Astronautica* 48: 707–710. https://doi.org/10.1016/S0094-5765(01)00078-9.

Collette, A., Sternovsky, Z., and Horanyi, M. 2014. Production of Neutral Gas by Micrometeoroid Impacts. *Icarus* 227: 89–93. https://doi.org/10.1016/j.icarus.2013.09.009.

Dalmann, B.-K., Grün, E., Kissel, J., and Dietzel, H. 1977. The Ion-Composition of the Plasma Produced by Impacts of Fast Dust Particles. *Planetary and Space Science* 25: 135–147. https://doi.org/10.1016/0032-0633(77)90017-4.

Daly, R. T., and Schultz, P. H. 2018. Projectile Preservation During Oblique Hypervelocity Impacts. *Meteoritics & Planetary Science* 53: 1364–90. https://doi.org/10.1111/maps.13081.

Davies, A. G. 2007. *Volcanism on Io: A Comparison with Earth*. Cambridge, UK: Cambridge University Press. https://doi.org/10.1017/CBO9781107279902.

Davies, A. G., Perry, J. E., Williams, D. A., Veeder, G. J., and Nelson, D. M. 2024. New Global Map of Io's Volcanic Thermal Emission and Discovery of Hemispherical Dichotomies. *The Planetary Science Journal* 5: 19. https://iopscience.iop.org/article/10.3847/PSJ/ad4346/pdf.

Davies, A. G., and Vorburger, A. H. 2022. Io's Volcanic Activity and Atmosphere. *Elements* 18: 379–384. https://doi.org/10.2138/gselements.18.6.379.

Davis, A. B., Guethe, C., Lopes, R. M. C., Hofmann, A. E., Turner, N., and Smythe, W. 2024. Prometheus: An Io Plume Sample Return Concept. 2024 IEEE Aerospace Conference, Big Sky, MT, USA, 1–12 https://doi.org/10.1109/AERO58975.2024.10521016.

Davison, T. M., Collins, G. S., Elbeshausen, D., Wünnemann, K., and Kearsley, A. 2011. Numerical Modeling of Oblique Hypervelocity Impacts on Strong Ductile Targets. *Meteoritics & Planetary Science* 46: 1510–24. https://doi.org/10.1111/j.1945-5100.2011.01246.x.

de Kleer, K., Hughes, E. C., Nimmo, F., Eiler, J., Hofman, A. E., Luszcz-Cook, S., and Mandt, K. 2024. Isotopic Evidence of Long-Lived Volcanism on Io. *Science* 384: 682–87. https://doi.org/10.1126/science.adj0625.

de Pater, I., Goldstein, D., and Lellouch, E. 2023. The Plumes and Atmosphere of Io. In *Io: A New View of Jupiter's Moon. Astrophysics and Space Science Library*, edited by R. M. C. Lopes, K. de Kleer, and J. Tuttle Keane, vol. 468. Cham: Springer. https://doi.org/10.1007/978-3-031-25670-7_8.

Della-Corte, V., et al. 2023. DISC – The Dust Impact Detector and Counter on-Board Comet Interceptor: Characterisation of the Dust Coma of a New Dynamically Active Comet. *Advances in Space Research* 71: 3457–67. https://doi.org/10.1016/j.asr.2023.01.049.

Destefanis, R., Schäfer, F., Lambert, M., and Faraud, M. 2006. Selecting Enhanced Space Debris Shields for Manned Spacecraft. *International Journal of Impact Engineering* 33: 219–230. https://doi.org/10.1016/j.ijimpeng.2006.09.065.

Dignam, A., Wozniakiewicz, P., Burchell, M., Alesbrook, L. S., Tighe, A., Suliga, A., Wessing, J., et al. 2022. Palladium-Coated Kapton for Use on Dust Detectors in Low Earth Orbit: Performance under Hypervelocity Impact and Atomic Oxygen Exposure. *Frontiers in Space Technology* 3: 933664. https://doi.org/10.3389/frspt.2022.933664.

Domínguez, G., Westphal, A. J., Phillips, M. L. F., and Jones, S. M. 2003. A Fluorescent Aerogel for Capture and Identification of Interplanetary and Interstellar Dust. *The Astrophysical Journal* 592: 631–35. https://iopscience.iop.org/article/10.1086/375549/pdf.

Drolshagen, G., McDonnell, J. A. M., Stevenson, T. J., Deshpande, S., Kay, L., Tanner, W. G., Mandeville, J. C., et al. 1996. Optical Survey of Micrometeoroid and Space Debris Impact Features on EURECA. *Planetary and Space Science* 44: 317–340. https://doi.org/10.1016/0032-0633(95)00140-9.

Fiege, K., Trieloff, M., Hillier, J. K., Guglielmino, M., Postberg, F., Srama, R., Kempf, S., and Blum, J. 2014. Calibration of Relative Sensitivity Factors for Impact Ionization Detectors with High-Velocity Silicate Microparticles. *Icarus* 241: 336–345. https://doi.org/10.1016/j.icarus.2014.07.015.

Fielding, L. A., Hillier, J. K., Burchell, M. J., and Armes, S. P. 2015. Space Science Applications for Conducting Polymer Particles: Synthetic Mimics for Cosmic Dust and Micrometeorites. *Chemical Communications* 51: 16886–99. https://doi.org/10.1039/C5CC07405C.

Fisher, C. R., Price, M. C., and Burchell, M. J. 2021. Salt Grains in Hypervelocity Impacts in the Laboratory: Methods to Sample Plumes from the Ice Worlds Enceladus and Europa. *Meteoritics & Planetary Science* 56: 1652–68. https://doi.org/10.1111/maps.13729.

Fitzgerald, H. J., and Yano, H. 1995. Micro-Abrasion Package Capture Cell Experiment on the Trailing Edge of LDEF: Impactor Chemistry and Whipple Bumper Shield Efficiencies. In *LDEF: 69 Months in Space. Third Post-Retrieval Symposium, Part 1, NASA-CP-3275-Pt-1*, edited by A. S. Levine, 455–457. Virginia, USA: NASA, Langley. https://ntrs.nasa.gov/citations/19950017376.

Foster, N., Wozniakiewicz, P. J., Price, M. C., Kearsley, A. T., and Burchell, M. J. 2013. Identification by Raman Spectroscopy of Mg–Fe Content of Olivine Samples after Impact at 6 Km $s^{-1}$ onto Aluminium Foil and Aerogel: In the Laboratory and in Wild-2 Cometary Samples. *Geochimica et Cosmochimica Acta* 121: 1–14. https://doi.org/10.1016/j.gca.2013.07.022.

Frank, L. A., and Paterson, W. R. 2002. Plasmas Observed with the Galileo Spacecraft During its Flyby Over Io's Northern Polar Region. *Journal of Geophysical Research, Space Physics* 107(A8): 31-1 – 31-18. https://doi.org/10.1029/2002JA009240.

Fujii, S., Armes, S. P., Jeans, R., Devonshire, R., Warren, S., McArthur, S. L., Burchell, M. J., Postberg, F., and Srama, R. 2006. Synthesis and Characterization of Polypyrrole-Coated Sulfur-Rich Latex Particles: New Synthetic Mimics for Sulfur-Based Micrometeorites. *Chemistry of Materials* 18: 2758–85. https://doi.org/10.1021/cm0601741.

Gardner, D. J., Collier, I., Shrine, N. R. G., Griffiths, A. D., and McDonnell, J. A. M. 1996. Micro-Particle Impact Flux on the Timeband Capture Cell Experiment of the Eureca Spacecraft. *Advances in Space Research* 17: 193–1999. https://doi.org/10.1016/0273-1177(95)00780-I.

Gault, D. E., and Wedekind, J. A. 1978. Experimental Studies of Oblique Impact. In *Proceedings of the 9th Lunar and Planetary Science Conference*, 3843–75. New York: Pergamon. https://adsabs.harvard.edu/full/1978LPSC....9.3843G.

Geissler, P. E., and McMillan, M. T. 2008. Galileo Observations of Volcanic Plumes on Io. *Icarus* 197: 505–518. https://doi.org/10.1016/j.icarus.2008.05.005.

Glavin, D. P., Dworkin, J. P., and Sandford, S. A. 2008. Detection of Cometary Amines in Samples Returned by Stardust. *Meteoritics & Planetary Science* 43: 399–413. https://doi.org/10.1111/j.1945-5100.2008.tb00629.x.

Goldsworthy, B. J., Burchell, M. J., Cole, M. J., Armes, S. P., Khan, M. A., Lascelles, S. F., Green, S. F., McDonnell, J. A. M., Srama, R., and Bigger, S. W. 2003. Time of Flight Mass Spectrometry of Ions in Plasmas Produced by Hypervelocity Impacts of Organic and Mineralogical Microparticles on a Cosmic Dust Analyser. *Astronomy & Astrophysics* 409: 1151–67. https://doi.org/10.1051/0004-6361:20031087.

Graham, G. A., Kearsley, A. T., Butterworth, A. L., Bland, P. A., Burchell, M. J., McPhail, D. S., Chater, R., Grady, M. M., and Wright, I. P. 2004. Extraction and Microanalysis of Cosmic Dust Captured During Sample Return Missions: Laboratory Simulations. *Advances in Space Research* 34: 2292–98. https://doi.org/10.1016/j.asr.2003.07.066.

Graham, G. A., Kearsley, A. T., Grady, M. M., Wright, I. P., Herbert, M. K., and McDonnell, J. A. M. 1999. Natural and Simulated Hypervelocity Impacts into Solar Cells. *International Journal of Impact Engineering* 23: 319–330. https://doi.org/10.1016/S0734-743X(99)00083-4.

Graham, G. A., Kearsley, A. T., Wright, I. P., Burchell, M. J., and Taylor, E. A. 2003. Observations on Hypervelocity Impact Damage Sustained by Multi-Layered Insulation Foils Exposed in Low Earth Orbit and Simulated in the Laboratory. *International Journal of Impact Engineering* 29: 307–316.

Graham, G. A., Kearsley, A. T., Wright, I. P., Grady, M. M., Drolshagen, G., McBride, N., Green, S. F., Burchell, M. J., Yano, H., and Elliot, R. 2001. Analysis of Impact Residues on Spacecraft: Possibilities and Problems https://adsabs.harvard.edu/full/2001ESASP.473..197G.In: Proceedings of the Third European Conference on Space Debris, 19–21 March 2001, Darmstadt, Germany. Ed.: Huguette Sawaya-Lacoste. ESA SP-473, Vol. 1, Noordwijk, Netherlands: ESA Publications Division, pp. 197–202

Graham, G. A., McBride, N., Kearsley, A. T., Drolshagen, G., Green, S. F., McDonnell, J. A. M., Grady, M. M., and Wright, I. P. 2001. The Chemistry of Micrometeoroid and Space Debris Remnants Captured on Hubble Space Telescope Solar Cells. *International Journal of Impact Engineering* 26: 263–274. https://doi.org/10.1016/S0734-743X(01)00087-2.

Graps, A., Grün, E., Svedhem, H., Graps, A. L., Krüger, H., Horányi, M., Heck, A., and Lammers, S. 2000. Io as a Source of the Jovian Dust Streams. *Nature* 405: 48–50. https://doi.org/10.1038/35011008.

Grasset, O., Dougherty, M. K., Coustenis, A., Bunce, E. J., Erd, C., Titov, D., Blanc, M., et al. 2013. JUpiter ICy Moons Explorer (JUICE): An ESA Mission to Orbit Ganymede and to Characterise the Jupiter System. *Planetary and Space Science* 78: 1–21. https://doi.org/10.1016/j.pss.2012.12.002.

Grün, E., Landgraf, M., Horányi, M., Kissel, J., Krüger, H., Srama, R., Svedhem, H., and Withnell, P. 2000. Techniques for Galactic Dust Measurements in the Heliosphere. *Journal of Geophysical Research* 105(A5): 10403–10. https://doi.org/10.1029/1999JA900376.

Grün, E., Zook, H., Baguhl, M., Zook, H. A., Balogh, A., Bame, S. J., Fechtig, H., et al. 1993. Discovery of Jovian

Dust Streams and Interstellar Grains by the Ulysses Spacecraft. *Nature* 362: 428–430. https://doi.org/10.1038/362428a0.

Hamann, C., Luther, R., Ebert, M., Hecht, L., Deutsch, A., Wünnemann, K., Schäffer, S., Osterholz, J., and Lexow, B. 2016. Correlating Laser-Generated Melts with Impact-Generated Melts: An Integrated Thermodynamic-Petrologic Approach. *Geophysical Research Letters* 43: 10,602–10,610. https://doi.org/10.1002/2016GL071050.

Harriss, K., and Burchell, M. J. 2016. A Study of the Observed Shift in the Peak Position of Olivine Raman Spectra as a Result of Shock Induced by Hypervelocity Impacts. *Meteoritics & Planetary Science* 51: 1289–1300. https://doi.org/10.1111/maps.12660.

Hillier, J. K., Postberg, F., Sestak, S., Srama, R., Kempf, S., Trieloff, M., Sternovsky, Z., and Green, S. F. 2012. Impact Ionization Mass Spectra of Anorthite Cosmic Dust Analogue Particles. *Journal of Geophysical Research* 117: E09002. https://doi.org/10.1029/2012JE004077.

Hillier, J. K., Sternovsky, Z., Kempf, S., Trieloff, M., Guglielmino, M., Postberg, F., and Price, M. C. 2018. Impact Ionisation Mass Spectrometry of Platinum-Coated Olivine and Magnesite-Dominated Cosmic Dust Analogues. *Planetary and Space Science* 156: 96–110. https://doi.org/10.1016/j.pss.2017.10.002.

Horányi, M., Kempf, S., Sternovsky, Z., Tucker, S., Pokorný, P., Turner, N. J., Castillo-Rogez, J. C., Bálint, T., West, J. L., and Szalay, J. R. 2019. Fragments from the Origins of the Solar System and our Interstellar Locale (FOSSIL): A Cometary, Asteroidal, and Interstellar Dust Mission Concept. 2019 IEEE Aerospace Conference, Big Sky, MT, USA, pp. 1–12 https://doi.org/10.1109/AERO.2019.8742223.

Hörz, F., Bastian, R., Borg, J., Bradley, J. P., Bridges, J. C., et al. 2006. Impact Features on the Stardust Collector and Implications for Wild 2 Coma Dust. *Science* 314: 1716–19. https://doi.org/10.1126/science.1135705.

Hörz, F., Zolensky, M. E., Bernhard, R. P., See, T. H., and Warren, J. L. 2000. Impact Features and Projectile Residues in Aerogel Exposed on Mir. *Icarus* 147: 559–579. https://doi.org/10.1006/icar.2000.6450.

Ishii, H., Brennan, S., Bradley, J. P., Pianetta, P., Kearsley, A. T., and Burchell, M. J. 2008. Sulfur Mobilization in Stardust impact tracks. *39th Lunar and Planetary Science Conference*, abstract #1561. https://www.lpi.usra.edu/meetings/lpsc2008/pdf/1561.pdf.

Johnson, J. R., Jaret, S. J., Glotch, T. D., and Sims, M. 2020. Raman and Infrared Microspectroscopy of Experimentally Shocked Basalts. *Journal of Geophysical Research: Planets* 125: e2019JE006240. https://doi.org/10.1029/2019JE006240.

Jones, S. M., Anderson, M. S., Davies, A. G., Kirby, J. P., Burchell, M. J., and Cole, M. J. 2015. Aerogel Dust Collection for In Situ Mass Spectrometry Analysis. *Icarus* 247: 71–76. https://doi.org/10.1016/j.icarus.2014.09.047.

Jones, S. M., and Flynn, G. J. 2006. Non-Silicate Aerogel as a Hypervelocity Particle Capture Material. *37th Lunar and Planetary Science Conference*, abstract #1852 https://www.lpi.usra.edu/meetings/lpsc2006/pdf/1852.pdf.

Jurewicz, A., Burnett, D., Wiens, R., Jurewicz, A. J. G., Burnett, D. S., Wiens, R. C., Friedmann, T. A., et al. 2003. The Genesis Solar-Wind Collector Materials. *Space Science Reviews* 105: 535–560. https://doi.org/10.1023/A:1024469927444.

Kadono, T., Niimi, R., Okudaira, K., Hasegawa, S., Tabata, M., and Tsuchiyama, A. 2012. Penetration into Low-Density Media: In Situ Observation of Penetration Process of Various Projectiles. *Icarus* 221: 587–592. https://doi.org/10.1016/j.icarus.2012.08.026.

Kearsley, A. T., Borg, J., Graham, G. A., Burchell, M. J., Cole, M. J., Leroux, H., Bridges, J. C., et al. 2008. Dust from Comet Wild 2: Interpreting Particle Size, Shape, Structure, and Composition from Impact Features on the Stardust Aluminum Foils 43: 41–73. https://doi.org/10.1111/j.1945-5100.2008.tb00609.x.

Kearsley, A. T., Drolshagen, G., McDonnell, J. A. M., Mandeville, J. C., and Moussi, A. 2005. Impacts on Hubble Space Telescope Solar Arrays: Discrimination between Natural and Man-Made Particles. *Advances in Space Research* 35: 1254–62. https://doi.org/10.1016/j.asr.2005.05.049.

Kearsley, A. T., and Graham, G. A. 2004. Multi-Layered Foil Capture of Micrometeoroids and Orbital Debris in Low Earth Orbit. *Advances in Space Research* 34: 939–943. https://doi.org/10.1023/A:1024469927444.

Kearsley, A. T., Graham, G. A., Burchell, M. J., Cole, M. J., Dai, Z., Teslich, N., Chater, R. J., Wozniakiewicz, P. J., Spratt, J., and Jones, G. 2007. Analytical Scanning and Transmission Electron Microscopy of Laboratory Impacts on Stardust Aluminium Foils: Interpreting Impact Crater Morphology and the Composition of Impact Residues. *Meteoritics & Planetary Science* 42: 191–210. https://doi.org/10.1111/j.1945-5100.2007.tb00227.x.

Kearsley, A. T., Graham, G. A., Burchell, M. J., Taylor, E. A., Drolshagen, G., Chater, R. J., and McPhail, D. 2005. Mulpex: A Compact Multi-Layered Polymer Foil Collector for Micrometeoroids and Orbital Debris. *Advances in Space Research* 35: 1270–81. https://doi.org/10.1016/j.asr.2005.03.030.

Kearsley, A. T., Webb, R. P., Grime, G. W., Wozniakiewicz, P. J., Price, M. C., Burchell, M. J., Salge, T., and Spratt, J. 2024. Cosmic Dust Impacts on the Hubble Space Telescope. *Philosophical Transactions of the Royal Society A* 382: 20230194. https://doi.org/10.1098/rsta.2023.0194.

Kempf, S., Tucker, S., Altobelli, N., Briois, C., Cable, M. L., Grün, E., Gudipati, M. S., et al. 2025. SUDA: A SUrface Dust Analyser for Compositional Mapping of the Galilean Moon Europa. *Space Science Reviews* 221: 10. https://doi.org/10.1007/s11214-025-01134-0.

Kissel, J., Brownlee, D. E., Büchler, K., Clark, B. C., Fechtig, H., Grün, E., Hornung, K., et al. 1986. Composition of Comet Halley Dust Particles from Giotto Observations. *Nature* 321: 336–37. https://doi.org/10.1038/321336a0.

Kissel, J., Glasmachers, A., Grün, E., Henkel, H., Höfner, H., Haerendel, G., von Hoerner, H., et al. 2003. Cometary and Interstellar Dust Analyzer for Comet Wild 2. *Journal of Geophysical Research* 108(E10): 8114. https://doi.org/10.1029/2003JE002091.

Kissel, J., and Krueger, F. R. 1987. Ion Formation by Impact of Fast Dust Particles and Comparison with Related Techniques. *Applied Physics A: Materials Science & Processing* 42: 69–85. https://doi.org/10.1007/BF00618161.

Kliore, A. J., Fjeldbo, G., Seidel, B. L., Sweetnam, D. N., Sesplaukis, T. T., Woiceshyn, P. M., and Rasool, S. I. 1975. The Atmosphere of Io from Pioneer 10 Radio Occultation Measurements. *Icarus* 24: 407–410. https://doi.org/10.1016/0019-1035(75)90057-3.

Kuebler, K. E., Jolliff, B. L., Wang, A., and Haskin, L. A. 2006. Extracting Olivine (Fo–Fa) Compositions from Raman Spectral Peak Positions. *Geochimica et Cosmochimica Acta* 70: 6201–22. https://doi.org/10.1016/j.gca.2006.07.035.

Laurance, M. R., and Brownlee, D. E. 1986. The Flux of Meteoroids and Orbital Space Debris Striking Satellites in Low Earth Orbit. *Nature* 323: 136–38. https://doi.org/10.1038/323136a0.

Leitner, J., Stephan, T., Kearsley, A. T., Hörz, F., Flynn, G. J., and Sandford, S. A. 2008. TOF-SIMS Analysis of Crater Residues from Wild 2 Cometary Particles on Stardust Aluminum Foil. *Meteoritics & Planetary Science* 43: 161–185. https://doi.org/10.1111/j.1945-5100.2008.tb00616.x.

Levine, A. S. 1993. LDEF: 69 Months in Space—3rd Post-Retrieval Symposium. NASA Conference Proceedings 3275 https://ntrs.nasa.gov/citations/19950017376.

Lopes, R.M.C., de Kleer, K., Keane, J.T. Introduction. In: Lopes, R.M.C., de Kleer, K., Tuttle Keane, J. (eds) *Io: A New View of Jupiter's Moon. Astrophysics and Space Science Library*, 468. Springer, Cham, 2023. https://doi.org/10.1007/978-3-031-25670-7_1.

Lorenz, R. D. 2015. Io Volcanic Plumes: Spacecraft Flythrough Hazard Evaluation. *Journal of Spacecraft and Rockets* 52: 990–93. https://doi.org/10.2514/1.A33188.

Love, S. G., and Brownlee, D. E. 1993. A Direct Measurement of the Terrestrial Mass Accretion Rate of Cosmic Dust. *Science* 262: 550–53. https://doi.org/10.1126/science.262.5133.550.

Maag, C. R., and Linder, W. K. 1992. Results of Space Shuttle Intact Particle Capture Experiments. In *Hypervelocity Impacts in Space*, 186–190. Canterbury: University of Kent at Canterbury.

Mandeville, J. C., and Bariteau, M. 2001. Cosmic Dust and Micro-Debris Measurements on the MIR Space Station. *Advances in Space Research* 28: 1317–24. https://doi.org/10.1016/S0273-1177(01)00403-3.

Marsh, S. P. 1980. *LASL Shock Hugoniot Data*, Vol. 658. Berkeley: University of California Press. http://large.stanford.edu/publications/coal/references/docs/shd.pdf.

McDonnell, J. A. M., Carey, W. C., and Dixon, D. G. 1984. Cosmic Dust Collection by the Capture Cell Technique on the Space Shuttle. *Nature* 309: 237–240. https://www.nature.com/articles/309237a0.pdf.

McDonnell, J. A. M., Drolshagen, G., Gardner, D. J., Aceti, R., and Collier, I. 1995. EURECA's Exposure in the Near Earth Space Environment. Hyper Velocity Impact Cratering Distributions at a Time of Space Debris Growth. *Advances in Space Research* 16: 73–83. https://doi.org/10.1016/0273-1177(95)98755-D.

McEwen, A. S., Haapala, A. F., Keszthelyi, L. P., and Mandt, K. E. 2023. Outstanding Questions and Future Observations of Io. In *Io: A New View of Jupiter's Moon. Astrophysics and Space Science Library*, edited by R. M. C. Lopes, K. de Kleer, and J. Tuttle Keane, vol. 468. Cham: Springer. https://doi.org/10.1007/978-3-031-25670-7_11.

McEwen, A. S., Keszthelyi, L., Spencer, J. R., Schubert, G., Matson, D. L., Lopes-Gautier, R., Klaasen, K. P., et al. 1998. High Temperature Silicate Volcanism on Jupiter's Moon Io. *Science* 281: 87–90. https://doi.org/10.1126/science.281.5373.87.

McEwen, A. S., Keszthelyi, L. P., Mandt, K. E., and the IVO Team. 2021. The Io Volcano Observer (IVO). *52nd Lunar and Planetary Science Conference (LPI Contrib. No. 2548)*, abstract #1352 https://www.hou.usra.edu/meetings/lpsc2021/pdf/1352.pdf.

McEwen, A. S., and Soderblom, L. 1983. Two Classes of Volcanic Plumes on Io. *Icarus* 58: 197–226. https://doi.org/10.1016/0019-1035(83)90075-1.

McKeegan, K. D., Aléon, J., Bradley, J., Brownlee, D., Busemann, H., Butterworth, A., Chaussidon, M., et al. 2006. Isotopic Compositions of Cometary Matter Returned by Stardust. *Science* 314: 1724–28. https://doi.org/10.1126/science.1135992.

Melosh, H. J. 2013. The Contact and Compression Stage of Impact Cratering. In *Impact Cratering: Processes and Products*, edited by G. R. Osinski, and E. Pierazzo, 32–42. West Sussex: Wiley-Blackwell, Chapter 3.

Meshik, A., Mabry, J., Hohenberg, C., Marrocchi, Y., Pravdivtseva, O., Burnett, D., Olinger, C., et al. 2007. Constraints on Neon and Argon Isotopic Fractionation in Solar Wind. *Science* 318: 433–35. https://doi.org/10.1126/science.1145528.

Mikula, R., Sternovsky, Z., Armes, S. P., Ayari, E., Bouwman, J., Chan, D. H. H., Fontanese, J., et al. 2024. Impact Ionization Mass Spectra of Polypyrrole-Coated Anthracene Microparticles: A Useful Mimic for Cosmic Polycyclic Aromatic Hydrocarbon Dust. *ACS Earth and Space Chemistry* 8: 586–605. https://pubs.acs.org/doi/10.1021/acsearthspacechem.3c00353.

Miller, M. E. C., Burke, S. E., and Continetti, R. E. 2022. Production and Impact Characterization of Enceladus Ice Grain Analogues. *ACS Earth and Space Chemistry* 6: 1813–22. https://doi.org/10.1021/acsearthspacechem.2c00354.

Morabito, L. A., Synnott, S. P., Kupferman, P. N., and Collins, S. A. 1979. Discovery of Currently Active Extraterrestrial Volcanism. *Science* 204: 972. https://doi.org/10.1126/science.204.4396.972.a.

Moussi, A., Drolshagen, G., McDonnell, J. A. M., Mandeville, J. C., Kearsley, A. T., and Ludwig, H. 2005. Hypervelocity Impacts on HST Solar Arrays and the Debris and Meteoroids Population. *Advances in Space Research* 35: 1243–53. https://doi.org/10.1016/j.asr.2005.03.060.

Nakazawa, S., Watanabe, S., Kato, M., Iijima, Y., Kobayashi, T., and Sekine, T. 1997. Hugoniot Equation of State of Basalt. *Planetary and Space Science* 45: 1489–92. https://doi.org/10.1016/S0032-0633(97)00070-6.

New, J. S., Mathies, R. A., Price, M. C., Cole, M. J., Golozar, M., Spathis, V., Burchell, M. J., and Butterworth, A. L. 2020. Characterizing Organic Particle Impacts on Inert Metal Surfaces: Foundations for Capturing Organic Molecules During Hypervelocity Transits of Enceladus Plumes. *Meteoritics & Planetary Science* 55: 465–479. https://doi.org/10.1111/maps.13448.

Niimi, R., Kadono, T., Arakawa, M., Yasui, M., Dohi, K., Nakamura, A. M., Iida, Y., and Tsuchiyama, A. 2011. In Situ Observation of Penetration Process in Silica Aerogel: Deceleration Mechanism of Hard Spherical Projectiles. *Icarus* 211: 986–992. https://doi.org/10.1016/j.icarus.2010.11.005.

Niimi, R., Kadono, T., Tsuchiyama, A., Okudaira, K., Hasegawa, S., Tabata, M., Watanabe, T., et al. 2012. Size and Density Estimation from Impact Track Morphology in Silica Aerogel: Application to Dust from Comet 81p/Wild 2. *The Astrophysical Journal* 744: 18. https://doi.org/10.1088/0004-637X/744/1/18.

Ogliore, R. C. 2023. Comet 81P/Wild 2: A Record of the Solar System's Wild Youth. *Geochemistry* 83: 126046. https://doi.org/10.1016/j.chemer.2023.126046.

Ogliore, R. C., Lopes, R. M. C., Hofmann, A. E., Turner, N. J., and Bolton, S. J. 2023. The Science Case for Io Sample Return. *54th Lunar and Planetary Science Conference*, abstract #1326 https://www.hou.usra.edu/meetings/lpsc2023/pdf/1326.pdf.

Ogliore, R. C., and Wilson, L. 2025. Size Distribution of Pyroclasts in Io's Prometheus Plume. *56th Lunar Planetary Science Conference*, abstract #1731.

Olivieri Lorenzo, L., Giacomuzzo, C., and Francesconi, A. 2024. Fragments Analysis of an Hypervelocity Impact Experiment on a Solar Array. *Acta Astronautica* 214: 316–323. https://doi.org/10.1016/j.actaastro.2023.10.044.

Ono, H., Kurosawa, K., Niihara, T., Mikouchi, T., Tomioka, N., Isa, J., Kagi, H., et al. 2023. Experimentally Shock-Induced Melt Veins in Basalt: Improving the Shock Classification of Eucrites. *Geophysical Research Letters* 50: e2022GL101009. https://doi.org/10.1029/2022GL101009.

Palma, R. L., Pepin, R. O., Westphal, A. J., Füri, E., Schlutter, D. J., Gainsforth, Z. S., and Frank, D. R. 2019. Helium and Neon in Comet 81P/Wild 2 Samples from the NASA Stardust Mission. *Meteoritics & Planetary Science* 54: 3–53. https://doi.org/10.1111/maps.13189.

Pappalardo, R. T., Buratti, B. J., Korth, H., Senske, D. A., Blaney, D. L., Blankenship, D. D., Burch, J. L., et al. 2024. Science Overview of the Europa Clipper Mission. *Space Science Reviews* 220: 40. https://doi.org/10.1007/s11214-024-01070-5.

Park, R. S., Jacobson, R. A., Gomez Casajus, L., Nimmo, F., Ermakov, A. I., Keane, J. T., McKinnon, W. B., et al. 2025. Io's Tidal Response Precludes a Shallow Magma Ocean. *Nature* 638: 69–73. https://doi.org/10.1038/s41586-024-08442-5.

Paul, K. G., Igenbergs, E. B., and Berthoud, L. 1997. Hypervelocity Impacts on Solar Cells—Observations, Experiments, and Empirical Scaling Laws. *International Journal of Impact Engineering* 20: 627–638. https://doi.org/10.1016/S0734-743X(97)87450-7.

Peale, S. J., Cassen, P., and Reynolds, R. T. 1979. Melting of Io by Tidal Dissipation. *Science* 203: 892–94. https://doi.org/10.1126/science.203.4383.892.

Perry, J., Lopes, R. M. C., Spencer, J. R., and Alexander, C. 2007. A Summary of the *Galileo* Mission and its Observations of Io. In *Io after* Galileo. Berlin, Heidelberg: Springer Praxis Books. Springer. https://doi.org/10.1007/978-3-540-48841-5_3.

Petkov, M. P., Jones, S. M., and Voecks, G. E. 2019. Zeolite-Loaded Aerogel as a Primary Vacuum Sorption Pump in Planetary Instruments. *Adsorption* 25: 187–200. https://doi.org/10.1007/s10450-018-00003-3.

Pierazzo, E., Artemieva, N. A., and Ivanov, B. A. 2005. Starting Conditions for Hydrothermal Systems underneath Martian Craters: Hydrocode Modeling. In *Large Meteorite Impacts III: Geological Society of America Special Paper 384*, edited by T. Kenkmann, F. Hörz, and A. Deutsch, 443–45. The Geological Society of America. https://doi.org/10.1130/0-8137-2384-1.443

Pierazzo, E., and Melosh, H. J. 2000a. Hydrocode Modeling of Oblique Impacts: The Fate of the Projectile. *Meteoritics & Planetary Science* 35: 117–130. https://doi.org/10.1111/j.1945-5100.2000.tb01979.x.

Pierazzo, E., and Melosh, H. J. 2000b. Understanding Oblique Impacts from Experiments, Observations, and Modelling. *Annual Review of Earth and Planetary Sciences* 28: 141–167. https://doi.org/10.1146/annurev.earth.28.1.141.

Pierazzo, E., and Melosh, H. J. 2000c. Melt Production in Oblique Impacts. *Icarus* 145: 252–261. https://doi.org/10.1006/icar.1999.6332.

Postberg, F., Hillier, J. K., Armes, S. P., Bugiel, S., Butterworth, A. L., Dupin, D., Fielding, L. A., et al. 2014. Stardust Interstellar Preliminary Examination IX: High Speed Interstellar Dust Analogue Capture in Stardust Flight-Spare Aerogel. *Meteoritics & Planetary Science* 49: 1666–79. https://doi.org/10.1111/maps.12173.

Postberg, F., Kempf, S., Srama, R., Green, S. G., Hillier, J. K., McBride, N., and Grün, E. 2006. Composition of Jovian Dust Stream Particles. *Icarus* 183: 122–134. https://doi.org/10.1016/j.icarus.2006.02.001.

Postberg, F., Khawaja, N., Abel, B., Choblet, G., Glein, C. R., Gudipati, M. S., Henderson, B. L., et al. 2018. Macromolecular Organic Compounds from the Depths of Enceladus. *Nature* 558: 564–68. https://doi.org/10.1038/s41586-018-0246-4.

Price, M. C., Hibbert, R., Arnold, D. C., Ramkissoon, N. K., Wozniakiewicz, P. J., Cole, M. J., and Burchell, M. J. 2014 European Planetary Science Congress 2014. Using Raman Mapping to Determine Hypervelocity Impact Peak Shock Pressures in High Purity Silicon, Germanium, Gallium Arsenide and Peridot Targets. EPSC Abstracts Vol. 9, EPSC2014-91 https://meetingorganizer.copernicus.org/EPSC2014/EPSC2014-91.pdf.

Price, M. C., Kearsley, A. T., and Burchell, M. J. 2013. Validation of the Preston–Tonks–Wallace Strength Model at Strain Rates Approaching $\sim 1011\ s^{-1}$ for Al-1100, Tantalum and Copper Using Hypervelocity Impact Crater Morphologies. *International Journal of Impact Engineering* 52: 1–10. https://doi.org/10.1016/j.ijimpeng.2012.09.001.

Price, M. C., Kearsley, A. T., Burchell, M. J., Hörz, F., Borg, J., Bridges, J. C., Cole, M. J., et al. 2010. Comet 81P/Wild 2: The Size Distribution of Finer (Sub-10 μm) Dust Collected by the Stardust Spacecraft. *Meteoritics & Planetary Science* 45: 1409–28. https://doi.org/10.1111/j.1945-5100.2010.01104.x.

Ratcliff, P. R., Burchell, M. J., Cole, M. J., Murphy, T. W., and Allahdadi, F. 1997. Experimental Measurements for Hypervelocity Impact Plasma Yield and Energetics. *International Journal of Impact Engineering* 20: 663–674. https://doi.org/10.1016/S0734-743X(97)87453-2.

Ratcliff, P. R., Reber, M., Cole, M. J., Murphy, T. W., and Tsembelis, K. 1997. Velocity Thresholds for Impact Plasma Production. *Advances in Space Research* 20: 1471–76. https://doi.org/10.1016/S0273-1177(97)00419-5.

Ryan, S., and Christiansen, E. 2013. Hypervelocity Impact Testing of Advanced Materials and Structures for Micrometeoroid and Orbital Debris Shielding. *Acta Astronautica* 83: 216–231. https://doi.org/10.1016/j.actaastro.2012.09.012.

Ryan, S., and Christiansen, E. 2015. Hypervelocity Impact Testing of Aluminum Foam Core Sandwich Panels. NASA/TM–2015–218593 https://doi.org/10.13140/RG.2.2.34366.09285.

Sato, M., Kurosawa, K., Kato, S., Ushioda, M., and Hasegawa, S. 2021. Shock Remanent Magnetization Intensity and Stability Distributions of Single-Domain Titanomagnetite-Bearing Basalt Sample under the Pressure

Range of 0.1–10 GPa. *Geophysical Research Letters* 48: e2021GL092716. https://doi.org/10.1029/2021GL092716.
Schultz, P. H., and Gault, D. E. 1990a. *Prolonged Global Catastrophes from Oblique Impacts*. Geological Society of America Special Paper 247, 239–261. The Geological Society of America. https://doi.org/10.1130/SPE247-p239
Schultz, P. H., and Gault, D. E. 1990b. Decapitated Impactors in the Laboratory and on the Planets. *21st Lunar and Planetary Science Conference*, 1099–1100. https://adsabs.harvard.edu/full/1990LPI....21.1099S.
Sekine, T., Kobayashi, T., Nishio, M., and Takahashi, E. 2008. Shock Equation of State of Basalt. *Earth, Planets and Space* 60: 999–1003. https://doi.org/10.1186/bf03352857.
Shrine, N. R. G., McDonnell, J. A. M., Burchell, M. J., Gardner, D. J., Jolly, H. S., Ratcliff, P. R., and Thomson, R. 1997. First Results from the Dustwatch-P Detectors of the European Space Exposure Facility. *Advances in Space Research* 20: 1481–84. https://doi.org/10.1016/S0273-1177(97)00421-3.
Simon, C. G., Hunter, J. L., Wortman, J. J., and Griffis, D. P. 1991. Ion Microprobe Elemental Analyses of Impact Features on Interplanetary Dust Experiment Sensor surfaces, LDEF-69 Months in Space—First Post-Retrieval Symposium, NASA CP3134 Pt I, 529–548 https://ntrs.nasa.gov/citations/19920014075.
Smith, B. A., Soderblom, L. A., Johnson, T. V., Ingersoll, A. P., Collins, S. A., Shoemaker, E. M., Hunt, G. E., et al. 1979. The Jupiter System through the Eyes of Voyager 1. *Science* 204: 951–972. https://doi.org/10.1126/science.204.4396.951.
Spencer, J. R., Stern, S. A., Cheng, A. F., Weaver, H. A., Reuter, D. C., Retherford, K., Lunsford, A., et al. 2007. Io Volcanism Seen by New Horizons: A Major Eruption of the Tvashtar Volcano. *Science* 318: 240–43. https://doi.org/10.1126/science.1147621.
Srama, R., Ahrens, T. J., Altobelli, N., Auer, S., Bradley, J. G., Burton, M., Dikarev, V. V., et al. 2004. The Cassini Cosmic Dust Analyzer. *Space Science Reviews* 114: 465–518. https://doi.org/10.1007/s11214-004-1435-z.
Stone, E. C., and Lane, A. L. 1979. Voyager 1 Encounter with the Jovian System. *Science* 204: 945–48. https://doi.org/10.1126/science.204.4396.945.
Strickson, O., and Artacho, E. 2016. Ab Initio Calculation of the Shock Hugoniot of Bulk Silicon. *Physical Review B* 93: 094107. https://doi.org/10.1103/PhysRevB.93.094107.
Tabata, M., Imai, E., Yano, H., Hashimoto, H., Kawai, H., Kawaguchi, Y., Kobayashi, K., et al. 2014. Design of A Silica-Aerogel-Based Cosmic Dust Collector for the Tanpopo Mission Aboard the International Space Station. *Transactions of the Japan Society for Aeronautical and Space Sciences, Aerospace Technology Japan* 12: 29–34. https://www.jstage.jst.go.jp/article/tastj/12/ists29/12_Pk_29/_pdf.
Tang, Q., He, Q., and Chen, X. 2024. Numerical Simulation Study on Mesoscopic Metallic Foam Core Sandwich Panels under Hypervelocity Impact. *Thin-Walled Structures* 195: 111440. https://doi.org/10.1016/j.tws.2023.111440.
Taylor, E. A., Scott, H. J., Abraham, M., and Kearsley, A. T. 2001. Hypervelocity Impact on Silicon Wafers with Metallic and Polymeric Coatings. In: Proceedings of the Third European Conference on Space Debris, 19–21 March 2001, Darmstadt, Germany. Ed.: Huguette Sawaya-Lacoste. ESA SP-473, Vol. 2, Noordwijk, Netherlands: ESA Publications Division, pp. 583–589. https://conference.sdo.esoc.esa.int/proceedings/sdc3/paper/47
Taylor, E. A., Tsembelis, K., Hayhurst, C. J., Kay, L., and Burchell, M. J. 1999. Hydrocode Modelling of Hypervelocity Impact on Brittle Materials. *Int. J. Impact Engng* 23: 895–904. https://doi.org/10.1016/S0734-743X(99)00133-5.
Timmermann, R., and Grün, E. 1991. Plasma Emission from High Velocity Impacts of Microparticles onto Water Ice. In *Origin and Evolution of Interplanetary Dust*, edited by A. C. Levasseur-Regourd, and H. Hasegawa, vol. 173, 375–78.Proceedings, 126th Colloquium of the International Astronomical Union. Dordrecht: Springer. https://doi.org/10.1007/978-94-011-3640-2_79
Trigo-Rodríguez, J., Domínguez, G., Burchell, M. J., Hörz, F., and Lorca, J. 2008. Bulbous Tracks Arising from Hypervelocity Capture in Aerogel. *Meteoritics & Planetary Science* 43: 75–86. https://doi.org/10.1111/j.1945-5100.2008.tb00610.x.
Tsou, P. 1995. Silica Aerogel Captures Cosmic Dust Intact. *Journal of Non-Crystalline Solids* 186: 415–427. https://doi.org/10.1016/0022-3093(95)00065-8.
Tsou, P., Brownlee, D. E., and Albee, A. 1984. Experiments on Intact Capture of Hypervelocity Particles. *15th Lunar Planetary Science Conference*, pp. 866–867 (abstract). https://articles.adsabs.harvard.edu/pdf/1984LPI....15..866T.
Tsou, P., Brownlee, D. E., Sandford, S. A., Hörz, F., and Zolensky, M. E. 2003. Wild 2 and Interstellar Sample Collection and Earth Return. *Journal of Geophysical Research* 108: 8113. https://doi.org/10.1029/2003JE002109.
Westphal, A. J., Flynn, G. J., Sutton, S. R., Bunch, T., Borg, J., Bibring, J. P., and Chardin, A. 1998. Identification and Chemical Composition of Particles Captured in Aerogel Flown on the MIR Spacestation. *39th Lunar and Planetary Science Conference* (abstracts), pp. 1917–1918.
Westphal, A. J., Snead, C., Butterworth, A., Graham, G. A., Bradley, J. P., Bajt, S., Grant, P. G., Bench, G., Brennan, S., and Pianetta, P. 2004. Aerogel Keystones: Extraction of Complete Hypervelocity Impact Events from Aerogel Collectors. *Meteoritics & Planetary Science* 39: 1375–86. https://doi.org/10.1111/j.1945-5100.2004.tb00952.x.
Westphal, A. J., Stroud, R. M., Bechtel, H. A., Brenker, F. E., Butterworth, A. L., Flynn, G. J., Frank, D. R., et al. 2014. Evidence for Seven Interstellar Origin of Seven Dust Particles Collected by the Stardust Spacecraft. *Science* 345: 786–791. https://doi.org/10.1126/science.1252496.
Wickham-Eade, J. E., Burchell, M. J., Price, M. C., and Harriss, K. H. 2018. Hypervelocity Impact Fragmentation of Basalt and Shale Projectiles. *Icarus* 311: 52–68. https://doi.org/10.1016/j.icarus.2018.03.017.
Williams, T. A., Parman, S. W., Saal, A. E., Akey, A. J., Gardener, J. A., and Ogliore, R. C. 2025. Lunar Volcanic Gas Cloud Chemistry: Constraints from Glass Bead Surface Sublimates. *Icarus* 438: 116607. https://doi.org/10.1016/j.icarus.2025.116607.
Wozniakiewicz, P. J., Bridges, J., Burchell, M. J., Carey, W., Carpenter, J., Della Corte, V., Dignam, A., et al. 2021. A Cosmic Dust Detection Suite for the Deep Space Gateway. *Advances in Space Research* 68: 85–104. https://doi.org/10.1016/j.asr.2021.04.002.
Wozniakiewicz, P. J., Ishii, H. A., Kearsley, A. T., Burchell, M. J., Bradley, J. P., Price, M. C., Teslich, N., Lee, M. R., and Cole, M. J. 2012. Stardust Impact Analogues: Resolving Pre- and Post-Impact Mineralogy in Stardust Al

Foils. *Meteoritics & Planetary Science* 47: 708–728. https://doi.org/10.1111/j.1945-5100.2012.01338.x.

Wozniakiewicz, P. J., Kearsley, A. T., Bridges, J., Holt, J., Price, M. C., Burchell, M. J., and Hicks, L. 2019. Orbital Dust Impact Experiment (ODIE)—A Passive Dust Collector Designed to Address the Dust Flux Data Gap. In First Int'l. Orbital Debris Conf. (Texas, USA: Lunar and Planetary Institute Universities Space Research Association National Aeronautics and Space Administration, 10. (LPI Contrib. No. 2109), abstract #6149 https://www.hou.usra.edu/meetings/orbitaldebris2019/orbital2019paper/pdf/6149.pdf.

Wozniakiewicz, P. J., Kearsley, A. T., Ishii, H. A., Burchell, M. J., Bradley, J. P., Teslich, N., Cole, M. J., and Price, M. C. 2012. The Origin of Crystalline Residues in Stardust Al Foils: Surviving Cometary Dust or Crystallized Impact Melts? *Meteoritics & Planetary Science* 47: 660–670. https://doi.org/10.1111/j.1945-5100.2011.01328.x.

Wozniakiewicz, P. J., Kearsley, A. T. K., Burchell, M. J., Price, M. C., Ishii, H. A., and Cole, M. J. 2018. Preparation of Large Aluminium Stardust Craters for Analysis. *Meteoritics & Planetary Science* 53: 1066–80. https://doi.org/10.1111/maps.13052.

Yamagishi, A., Hashimoto, H., Yano, H., Imai, E., Tabata, M., Higashide, M., and Okudaira, K. 2021. Four-Year Operation of Tanpopo: Astrobiology Exposure and Micrometeoroid Capture Experiments on the JEM Exposed Facility of the International Space Station. *Astrobiology* 21: 1461–72. https://doi.org/10.1089/ast.2020.2430.

Yano, H., Collier, I., Shrine, N., and McDonnell, J. A. M. 1996. Microscopic and Chemical Analyses of Major Impact Sites on Timeband Capture Cell Experiment of the Eureca Spacecraft. *Advances in Space Research* 17: 189–192. https://doi.org/10.1016/0273-1177(95)00779-E.

Yano, H., Kibe, S., Deshpande, S. P., and Neish, M. J. 1997. The First Results of Meteoroid and Debris Impact Analyses on Space Flyer Unit. *Advances in Space Research* 20: 1489–94. https://doi.org/10.1016/S0273-1177(97)00423-7.

Zhao, L., Wang, H., Fu S. Zhao, C., and Wu, Y. 2025. A Theoretical Model for Estimating Hypervelocity Impact Generated Plasma (HVIGP) Considering Phase Transitions. *International Journal of Impact Engineering* 203: 105341. https://doi.org/10.1016/j.ijimpeng.2025.105341.

Zolensky, M. E., Pieters, C., Clark, B., and Papike, J. J. 2000. Small Is Beautiful: The Analysis of Nanogram-Sized Astromaterials. *Meteoritics & Planetary Science* 35: 9–29. https://doi.org/10.1111/j.1945-5100.2000.tb01970.x.

Zolensky, M. E., Zega, T. J., Yano, H., Wirick, S., Westphal, A. J., Weisberg, M. K., Weber, I., et al. 2006. Mineralogy and Petrology of Comet 81P/Wild 2 Nucleus Samples. *Science* 314: 1735–39. https://doi.org/10.1126/science.1135842.